Stabilization of low-altitude balloon systems, Part 2: riggings with multiple taut ground tethers, analyzed as tensegrity systems

Thomas Bewley, UC San Diego and NASA Jet Propulsion Laboratory

November 2, 2021

Abstract

The paper considers the rigging of low-altitude balloon/payload systems with multiple taut ground tethers, analyzed as tensegrity systems. The statics and dynamics of tensegrity systems with fixed nodes, applied external loads, and embedded solid bodies is first reviewed. We identify and consider a handful of wobbly rigging designs, W1-W3, each with infinitesimal mechanisms associated with zero deformation energy of the structure (a.k.a. soft modes), as well as a number of stable rigging designs, S1-S6, each with no such infinitesimal mechanisms. Design S1 is statically determinant, with the applied loads uniquely determining the tensions in the tethers. Designs S2-S6 are not pretensionable, but are still tensionable under load: after the nominal balloon lift and payload weight are applied, there are a few (\bar{n}) remaining degrees of freedom. Once the static tension in \bar{n} control tethers is set, the resulting tension in the remaining tethers, due to the (known) nominal loads plus the (unknown) disturbance loads, is uniquely determined. A strategy for tuning the static tension in the \bar{n} control tethers is proposed which, in a sense, maximizes the range of unsteady disturbance loads that the tensegrity system can endure before one of the tethers in the system goes slack. A block-and-tackle (pulley) mechanism with fractional mechanical advantage (MA1.5) is introduced to equalize the tension in three adjacent tethers in Design S6. To facilitate the close and sustained inspection of interesting features on cliffs, stable rigging designs C1-C3 are also proposed, each of which is designed to straddle a cliff, with some ground attachment points at the foot of the cliff and some at the top.

1 Introduction

As summarized in the abstract, this paper considers the practical problem of designing a rigging (that is, a 3D network of tensile members, a.k.a. strings or tethers¹, including a number of tethers anchored to three or more attachment points on the ground) to stabilize a low-altitude balloon/payload system. The ground attachment points may be fixed in position, or mounted atop sufficiently heavy rovers which may be moved as needed. As compared with the use of a single ground tether, which is considered in a companion paper [1], the appropriate use of multiple tethers to secure a (buoyant) balloon and its (heavy) payload to fixed or mobile ground attachment points can diminish significantly the deflections in both position and orientation of both the balloon and the payload hanging below it in the presence of variable winds.

If the multiple ground tethers are attached to a single common point at or below the base of the balloon, while the center of pressure modeling the net effect of the wind forces acting on the balloon is close to the balloon center, the balloon will tend to translate and pitch significantly in response to unsteady winds and/or vortex shedding past the balloon—at times, even making certain downwind tethers go slack, thereby putting highly undesirable timevarying loads (i.e., "jerks") on the balloon and payload every time a slack tether again becomes taut. The ground tethers in such problems are thus generally tied off at 3 or 4 (or more) attachment points on the *sides* of the balloon (at its equator, or slightly below). As we will show, simple intuition often fails dramatically when attempting to interconnect these attachment points on the balloon to those on the ground and the payload in order to stabilize the entire system in the presence of variable winds; proper analysis is thus essential.

The present paper takes a distinctly utilitarian perspective on the practical problem of stabilizing balloon/payload systems with multiple taut ground tethers, while at the same time leveraging the powerful and streamlined analysis framework of tensegrity systems laid out in the seminal work of [16]. Towards this end, we will focus almost exclusively (with the exception of an initial illustratory 2D implementation of Design W1) on the 3D case, and focus on rigging designs with 3 to 8 ground attachment points, and 3 to 4 attachment points on both the balloon and the payload.

¹We will call the tensile members "strings" in §3, as is standard in the literature on tensegrity systems, and we will call them "tethers" elsewhere, as is standard in the literature on ballooning.



Figure 1: Commercially available aerostats from (left) SkyDoc and (right) Lindstrand. The SkyDoc balloon shown here happens to be rigged as in Figure 3a; much better rigging designs are proposed in §4.2.1-4.2.3.

Balloons that are designed specifically to be operated in a tethered configuration, via various different types of aerodynamic streamlining, are often referred to as aerostats. Commercially available aerostats come in many different sizes and shapes (some of which are patent encumbered), all of which are designed to minimize (but unfortunately do not eliminate) perturbations under variable winds. The present study is focused around simple spherical or ellipsoidal balloons (like the SkyDoc Model 18 shown in Figure 1), but could be extended to many different aerostats. The SkyDoc Model 18 is an ellipsoidal balloon with a small fabric drogue chute of sorts slung on its underside along its downwind perimeter, implemented to provide a constant drag on the balloon in the presence of a prevailing wind in an attempt to "anchor" its position in space with the force of the wind itself. The SkyDoc Model 18 is 4.33m in diameter by 2.80m in height, with 3.5mil plastic walls, and requires 27.22m³ of Helium to fill, giving it a net lift of 17.17 kg at sea level. The similarly-sized Raven Aerostar TIF-1600 is blimp shaped, 9.6m in length and 3.3m in diameter with a net lift of 16 kg at sea level.

Typical payloads for current airborne platforms suspended from tethered balloons include narrow field-of-view cameras and radio antennas. Such instruments need to be pointed accurately (+/- a few degrees in pitch, roll, and yaw) in order to perform their assigned functions correctly. While commercial-off-the-shelf (COTS) motorized gimbal stabilizers can further augment the stability of such cameras and antennas somewhat, they often come with a substantial weight penalty. A relatively stable balloon-suspended platform for mounting such payloads thus provides the essential starting point. This paper focuses on how to configure the rigging of such a system in order to best achieve this stability. The structure of the paper is as follows:

§1.1-§1.2 introduce potential applications of tethered balloons for cliff exploration and solar energy collection;

§1.3-§1.4 review the available tether and hull material, and relevant lift gas performance on Earth, Mars, and Titan²; §2 performs a simple analysis to estimate the minimum balloon size required to stabilize a balloon/payload system in the presence of a prevailing wind of a given maximum speed;

§3.1 reviews the conditions of static equilibrium of general tensegrity structures, including how to identify infinitesimal modes, and how to tune the tensions in the strings when the conditions of static equilibrium are underdetermined via solution of an LP;

§3.2 reviews the equations governing the dynamics of class 1 tensegrity structures with embedded solid bodies; §4 proposes and characterizes numerous rigging designs for balloon/payload systems, the tensions of which may be optimized with the techniques of §3.1, and the dynamics of which may be modelled using the techniques of §3.2; §4.5 then outlines some forthcoming next steps.

1.1 Cliff exploration using tethered balloon observation platforms

Much of the rich geological history on Earth and other planetary bodies is best revealed in the highly stratified sedimentary rocks exposed in steep cliffs, such as the remarkable Valles Marineris region of Mars. In addition, certain unique biological specimens on Earth, and noteworthy transient environmental features on Mars, also occur only

²In contrast with (untethered) high altitude balloons [20, 5, 17, 13, 8], opportunities for tethered balloon operation near the surface of planetary bodies in our solar system other than Earth, Mars, and Titan (a moon of Saturn) are essentially zero. The surface temperature of Venus is far too high (at 467°C, it is hot enough to melt lead). The pressure at the "surface" (to the extent that one can be distinguished) of the gas giants (Jupiter, Saturn, Uranus, & Neptune) is far too high. The atmospheric pressure at the surface of Neptune's moon Triton is currently estimated as only 1/20,000 of an Earth atmosphere, and the other planets, dwarf planets, and moons in the solar system either have an atmosphere far thinner than Triton, or have no atmosphere at all.

within cliffs and steep tallus slopes. Particular objects of interest include various nesting areas and rare vegetation on Earth (e.g., the ancient dioecious herb *Borderea chouardii* in the Spanish Pyrenees [7]), and the occasional bright gully deposits in the western region of Hale Crater [9]; studies of such phenomena are instrumental in the search for liquid water on or near the surface of Mars.

Substantial ongoing research is thus devoted to the autonomous exploration of steep cliffs, primarily using vehicles that either free climb from below using advanced rock grippers (e.g., JPL's Limbed Excursion Mechanical Utility Robot [2]), or descend from above via controlled rappel (e.g., Caltech's tethered two-wheeled Axel rover [14]). Unfortunately, both free climbing (up from below) and rappelling (down from above) are highly delicate maneuvers, with potentially dire consequences (both to the robot, and to the delicate biological objects or environmental features under consideration) for any misstep. The JPL Mars 2020 mission thus introduced the remote operation of an unmanned helicopter (a.k.a. drone) on Mars, albeit with a 3 minute maximum mission duration. Such drones might also be considered for further exploration of interesting areas unreachable by conventional rovers; however, with their extremely limited payload capacity and mission duration, the extent of the remote exploration that drones can be expected to perform on Mars is anticipated to be quite limited.

Remarkably, many otherwise difficult-to-reach areas (cliffs, tallus slopes, crater walls, sinkholes, etc) on Earth, Mars, and Titan are readily made safely accessible for sustained close inspection (imaging, sampling, drilling, etc) by stabilized measurement platforms suspended from stably tethered balloons.

The problem of remotely deploying such a multiply-tethered balloon system is an interesting (and, it appears, solvable) challenge. The main rover, responsible for initially filling and deploying the balloon and its payload (and, safely lowering and/or stowing them again when storms threaten), can be positioned at either the top or bottom of the cliff, whichever is easier. The auxiliary rovers, responsible for anchoring the other ground tethers when the system is deployed, might ultimately have to travel significant distances from the main rover in order to reach their desired anchor points. Once all rovers are in position (and, when the wind is low), a dextrous drone can be used to connect the tethers between the (partially-deployed) balloon/payload system and the auxiliary rovers; the numerous details of such a deployment strategy, which would in part leverage advanced semi-slack tether management techniques such as those discussed in [18], is deferred to future work. Note finally that rovers need not be used at every anchor point. In certain instances, tubular Nylon webbing or cord (made, e.g., from Perlon™, a brand of abraison-resistant Nylon fiber by I.G. Farben), slung around an existing rock feature and appropriately secured (as done frequently by rock climbers) would be sufficient. Developing an autonomous drone that is precise and dextrous enough to secure such a sling around a rock, to provide a tether anchor point within a talus slope littered with rocks of various sizes, is a robotics/drone coordination challenge that appears to be within reach.

1.2 Concentrated photovoltaic (CPV) collection of solar energy with balloons

In the early 2000s, Cool Earth Solar pioneered the development of tethered balloons designed to act as low-cost concentrated photovoltaic (CPV) solar collectors on Earth. These balloons were characterized by a transparent upper surface, a reflective lower surface, and a small, high-efficiency solar panel at the focal point (on the inside of the upper surface of the balloon), with the power collected by this solar panel transmitted down one of the tethers, which were also used to aim the (air-filled) balloons appropriately, tracking the sun. This investigation leveraged \$21M in angel investments and venture funding, and led to a follow-on 5-year cooperative research and development agreement (CRADA) in 2013 with Sandia National Labs to develop related low-cost solar technologies.

The active development of low-cost air-filled solar balloons for use on Earth, as originally envisioned by Cool Earth Solar, has since wound down. However, this essential idea, duly made more robust for reliable remote operation, may (speculatively) be considered for possible use in the buoyant setting described in §1.1, thereby achieving dual use of the large balloon that would be needed (that is, the balloon used could both hoist the payload in a stable fashion, and collect solar energy³). In such a dual-use setting, the multiple-tether rigging system would be used both to track the sun, by aiming the CPV balloon system appropriately, as well as to reject perturbations to the orientation of the payload, due both to wind disturbances as well as to the continuous reaiming of the CPV balloon.

Alternatively, the lower surface of the tethered balloon, which can be made nearly parabolic in shape, might instead be used, in a similar fashion, as an antenna to transmit signals to orbit, or all the way back to Earth.

1.3 Tether and hull material

Remarkably strong and lightweight COTS fibers are available today for use in multi-tethered balloon operations, notably including Spectra[™] and Dyneema[™] (two brands of Ultra-High Molecular Weight Polyethylene, by Honeywell

³This idea is natural on Earth and Mars; as the solar flux at the surface of Mars is about 43% that on Earth. This idea is quite dubious on Titan, however, where the solar flux at the surface is only about 0.1% that on Earth.

H_2	Не	Atmosphere on Earth	Atmosphere on Mars	Atmosphere on Titan
2.016	4.003	28.96	43.34	28.5

Table 1: Molecular mass M_{qas} of five relevant gases, in units of [g/mol] (divide by 1000 for [kg/mol]).

				kinematic	densities [kg/m ³]				
	pressure	temperature	gravity	vity viscocity atmosphere		H ₂ balloon		He balloon	
	P_{atm} [Pa]	$T \ [^{\circ} \mathrm{K}]$	$g [\mathrm{m/s^2}]$	$\nu_{atm} [\mathrm{m}^2/\mathrm{s}]$	$ ho_{atm}$	$ ho_{ m H_2}$	lift	$ ho_{ m He}$	lift
Earth	101300	288	9.80	1.48e-5	1.225	0.087	1.138	0.173	1.052
Mars	600	210	3.71	0.0011	0.0149	0.00071	0.0142	0.00140	0.0135
Titan	146700	95	1.35	1e-6	5.293	0.382	4.911	0.758	4.535

Table 2: Typical atmospheric characteristics, and H_2 and H_2 and H_3 and H_4 and H_4 and H_5 are surface of Earth, Mars, and Titan [SI units]. The atmospheric density is computed via $\rho_{atm} = P_{atm} \, M_{gas}/(R_u \, T)$, noting Table 1, where $R_u = 8.31446 \, [\mathrm{J/(mol~K)}]$ is the universal gas constant. The H_2 and H_4 balloon densities are computed similarly, assuming 2% overpressure in the balloon; i.e., the gas pressure in the balloon is taken as $(1.02 \, P_{atm})$. Neglecting the weight W_{hull} of the material forming the surface of the balloon, the relative contribution of which diminishes as the balloon is made larger (see §2), the lift capacity of each balloon is simply the atmospheric density minus the corresponding gas density in that balloon; the corresponding lift force is the lift capacity times the volume of the balloon and the local value of g.

and DSM respectively) and Kevlar[™] (a brand of synthetic aromatic polyamide by DuPont). All three fibers are available as braided lines in a wide variety of diameters; at 0.7 mm diameter, they are all generally around 0.25 lbs per 1000 ft [0.37 kg per 1000 m] with 100-150 lbs [50-70 N] breaking strength and about 2% stretch at breaking. Braids made with such fibers vary in their abrasion, moisture, and chemical resistance, as well as their low-temperature embrittlement; these properties would ultimately govern which particular fiber type is best suited for use as tethers in any given application. More speculatively, the future development (specifically, for "space elevators") of carbon nanotubes as an even stronger/lighter replacement for such braided polymer fibers is also being explored. Lightweight coaxial tethers can also be implemented to carry both power and signal in addition to bearing load, as discussed further in [18].

Numerous COTS inflatable textile and polymeric materials are available today for forming the hull, or surface, of the aerostat. These composite materials are generally formed as several layers bonded together. An essential inner layer provides a barrier with very low permeability to the lift gas; other layers provide strength, tear resistance, and environmental protection (against ultraviolet light, ozone, humidity, etc). These several functional layers are joined with adhesive layers that bond extremely well with adjacent layers to form a multi-layer flexible laminate that is resistant to fatigue from flexing during both normal operation as well as the inflation/deflation process. For a recent review of such materials, see [4]. Typical polymeric hull material is about 4 mil [0.1 mm] thick and about 0.1 kg/m².

1.4 Lift gas: helium versus hydrogen in deployments on Earth, Mars, or Titan

The balloon itself can be filled with either helium or hydrogen; as seen in Tables 1 and 2, the lift capacity of either is within 8% of the other. Note further that, as compared to a deployment on Earth with a payload of a given mass, a much larger $(78 \times$ the volume, or $4.3 \times$ the diameter) balloon is required to lift this payload on the surface of Mars (due primrily to its thinner atmosphere), whereas a smaller $(0.23 \times$ the volume, or $0.61 \times$ the diameter) balloon is sufficient to lift this payload on Titan (due primarily to its colder temperature).

Note that, in a collaborative effort between several NASA centers, a large effort is currently underway to synthesize hydrogen (stored as methane) and oxygen from the atmosphere and regolith on Mars, in an activity dubbed "dust to thrust" [19]. If such a system is one day successfully developed and delivered to Mars, hydrogen for filling such balloons might one day be produced directly on the surface of Mars itself, thereby facilitating large-scale deployments⁴.

⁴Of course, if both filling the balloon with hydrogen and using the balloon to collect solar energy, one needs to be exceptionally careful with both the heat and the electricity generated, lest the balloon become a Martian (or, Titanian) Hindenburg.

2 Preliminary balloon sizing

In §4, we propose a variety of rigging designs for stabilizing a balloon/payload system at a target payload height H. To set up fair quantitative comparisons of these designs in a planned follow-up paper, using both the analysis techniques for the statics and dynamics of tensegrity systems laid out in §3 as well as corresponding balloon experiments, all designs considered will restrict the locations of the fixed nodes on the ground to lie within a circle of some radius R; a few different values of R/H will be considered. We also denote by r the radius of the balloon (assumed initially to be nearly spherical), and by h the vertical distance between the center of the balloon and the center of the payload. We perform some preliminary computations here to estimate the required balloon size.

As discussed in §1.4, the balloon lift is $L = (\rho_{\rm atm} - \rho_{\rm lift.gas}) g \, 4\pi r^3/3 \propto r^3$. Consider the presence of a horizontal wind of maximum speed w, and identify the balloon Reynolds number $Re = 2rw/\nu_{atm}$, where ν_{atm} is given in Table 2. The drag of the balloon in the presence of this wind is $D = C_d \, \rho_{\rm atm} \, \pi r^2 \, w^2/2 \propto r^2 w^2$, where $C_d \approx 0.2$ for $Re \gtrsim 10^6$ (that is, in the post-critical separated flow regime with a turbulent boundary layer over a smooth balloon surface). Define also the excess lift, $E = L - W_{\rm hull} - W_{\rm tethers} - W_{\rm payload}$, as the lift L of the balloon minus the weight of the fabric forming the balloon surface, $W_{\rm hull} = \rho_{\rm hull} \, 4\pi r^2$, the weight of the rigging, $W_{\rm tethers} = p \, \rho_{\rm tethers} \sqrt{R^2 + H^2}$ (where p is the number of ground tethers used), and the (given) weight of the payload, $W_{\rm payload}$.

To simplify the analysis, consider first a 2D setting in which r and h are small compared to R and H. In this case, the two outer tethers between the balloon and the ground form an isosceles triangle, with the angle γ at its top vertex satisfying $\gamma/2 = \operatorname{atan}(R/H)$. Analyzing the force vector at this vertex, it is plainly evident that both tethers in this setting will stay in tension, with the upwind tether carrying progressively higher tension compared to the downwind tether as the wind speed w is increased, until the ratio D/E of the horizontal to (total) vertical forces at this vertex reach the proportion R/H; that is, until

$$\frac{R}{H} = \frac{D}{E} = \frac{C_d \,\rho_{\text{atm}} \,\pi r^2 \,w^2 / 2}{(\rho_{\text{atm}} - \rho_{\text{lift,gas}}) \,g \,4\pi r^3 / 3 - \rho_{\text{hull}} \,4\pi r^2 - p \,\rho_{\text{tethers}} \sqrt{R^2 + H^2} - W_{\text{payload}}},\tag{1}$$

at which point the downwind tether goes slack. Note that, for a given maximum wind speed w, the drag-to-lift ratio $D/L \propto 1/r$ is reduced as r is increased. For r that is too small, the balloon lift is barely sufficient to hoist the payload, and the denominator on the RHS of (1) is small; increasing r, the lift term in the denominator on the RHS grows faster than both the numerator and the other terms in the denominator, and a balance in (1) is eventually reached. For a given target H, an intermediate R/H is generally necessary, as larger R/H require longer tethers, which risk sagging and fouling, and smaller R/H require a larger balloon radius r, by (1). Once the geometric factor R/H is chosen for a given payload weight $W_{\rm payload}$, a given payload height H, and a specified maximum horizontal wind speed w, an appropriate minimum balloon radius r may be selected simply by solving (1). For example, taking R/H = 1 (i.e., taking $\gamma/2 = 45^{\circ}$), $\rho_{\rm atm} = 1.225 \, {\rm kg/m^3}$ and $\rho_{\rm atm} - \rho_{\rm He} = 1.052 \, {\rm kg/m^3}$ (see Table 2), $\rho_{\rm hull} \approx 0.1 \, {\rm kg/m^2}$ and $\rho_{\rm tethers} = 0.37 \cdot 10^{-3} \, {\rm kg/m}$ (see §1.3), p = 2 ground tethers, $W_{\rm payload} = 98 \, {\rm N}$, $H = 30 \, {\rm m}$, and a max wind speed of $w = 13 \, {\rm m/s}$ (25 knots), we arrive at $r = 2.1 \, {\rm m}$ (similar in size to the SkyDoc Model 18) and Re = 3.6e6. The starting point in developing a balloon/payload system that is stable in the presence of winds is thus:

- (a) designing the lightest possible payload (i.e., minimizing $W_{\rm payload}$), while
- (b) selecting a streamlined balloon shape (e.g., ellipsoid or blimp shaped, both of which are better than spherical) to minimize the drag D in the presence of wind. A blimp shape is appropriate if the prevailing wind direction is nearly constant and known in advance, so the balloon can be aimed into the wind by the tethers, whereas an ellipsoid is more versatile in the presence of winds that are anticipated to be variable in direction.

Once the payload weight W_{payload} , balloon shape and corresponding drag formula, and tether geometric factor R/H are selected, an appropriate balloon size r may then be selected as in (1), as shown in the example above.

Note that, for $\rho_{\text{lift-gas}} \ll \rho_{\text{atm}}$ and sufficiently large r (so that $E \approx L$),

$$\frac{D}{E} \approx \frac{3 C_d}{8} \frac{w^2}{g r} \propto \frac{w^2}{g r} = F r^2,$$

where we identify $Fr = w/\sqrt{gr}$ as the Froude number of the balloon; to leading order, the balloon radius r should be sized such that $Fr \leq O(1)$ for the balloon system to be stabilizable with ground tethers for a given wind speed w.

For 3D implementations, the p points on the ground form a regular polygon of circumradius R. For p = 3, these points form an equilateral triangle with inradius $R_{\rm in} = R/2$, whereas for p = 4 they form a square with inradius $R_{\rm in} = R/\sqrt{2}$. In the 3D case, the minimum balloon size r may be selected via (1) as discussed previously in the 2D case if the prevailing wind direction is known (so that a tether may be oriented in the upwind direction); if the prevailing wind direction is unknown, however, the worst case may be considered by taking the upwind direction as halfway between the tether directions, and the formula given in (1) should thus replace R with $R_{\rm in}$; it is seen in this setting that fourfold symmetry pays a significantly lower penalty than threefold symmetry $(1/\sqrt{2} \text{ rather than } 1/2)$.

3 Analysis of tensegrity systems

3.1 Static equilibrrum of tensegrity structures with fixed nodes and external forces

Following the analysis of the static equilibrium of tensegrity structures in chapter 2 of [16], augmenting its notation slightly as necessary, consider a 2D or 3D structure with:

- q free nodes $\{\vec{q}_1,\ldots,\vec{q}_q\}$ and p fixed nodes $\{\vec{p}_1,\ldots,\vec{p}_p\}$, collectively called the n=q+p nodes $\{\vec{n}_1,\ldots,\vec{n}_n\}$, and
- $b \ \underline{b} ars \ \{\vec{b}_1, \ldots, \vec{b}_b\}$ and $s \ \underline{s} trings \ \{\vec{s}_1, \ldots, \vec{s}_s\}$, collectively called the $m = b + s \ \underline{m} embers \ \{\vec{m}_1, \ldots, \vec{m}_m\}$.

For the purpose of analyzing static equilibria in §3.1, solid bodies with n attachment points will be modelled simply as clusters of n(n-1)/2 interconnected bars (i.e., with one bar between each two points on the body); this model is refined in order to account properly for solid-body dynamics in §3.2. The nodal locations \vec{n}_i are each vectors from the origin in \mathbb{R}^d , where d=2 or 3 is the dimension of the problem considered, and are denoted as follows⁵:

$$Q = \begin{bmatrix} \vec{q}_1 & \cdots & \vec{q}_q \end{bmatrix}, \quad \mathbf{q} = \text{vec}(Q) = \begin{bmatrix} \vec{q}_1 \\ \vdots \\ \vec{q}_q \end{bmatrix}, \quad P = \begin{bmatrix} \vec{p}_1 & \cdots & \vec{p}_p \end{bmatrix}, \quad \mathbf{p} = \text{vec}(P) = \begin{bmatrix} \vec{p}_1 \\ \vdots \\ \vec{p}_n \end{bmatrix}$$

$$\Rightarrow \quad \begin{bmatrix} Q & P \end{bmatrix} = N = \begin{bmatrix} \vec{n}_1 & \cdots & \vec{n}_n \end{bmatrix}, \quad \mathbf{n} = \begin{bmatrix} \mathbf{q} \\ \mathbf{p} \end{bmatrix} = \text{vec}(\begin{bmatrix} Q & P \end{bmatrix}); \tag{2a}$$

q and Q, which define the locations of the free nodes, are sometimes called the *configuration vector* and *configuration matrix*, respectively, of the tensegrity structure. Each member $\vec{m}_k = \vec{n}_{k,1} - \vec{n}_{k,2}$ connects two nodes, $\vec{n}_{k,1}$ and $\vec{n}_{k,2}$, at least one of which is free (e.g., in Figure 2, $\vec{m}_1 = \vec{b}_1 = \vec{n}_2 - \vec{n}_1 = \vec{q}_2 - \vec{q}_1$), and are denoted as follows:

$$B = \begin{bmatrix} \vec{b}_1 & \cdots & \vec{b}_b \end{bmatrix}, \quad \mathbf{b} = \text{vec}(B) = \begin{bmatrix} \vec{b}_1 \\ \vdots \\ \vec{b}_b \end{bmatrix}, \quad S = \begin{bmatrix} \vec{s}_1 & \cdots & \vec{s}_s \end{bmatrix}, \quad \mathbf{s} = \text{vec}(S) = \begin{bmatrix} \vec{s}_1 \\ \vdots \\ \vec{s}_s \end{bmatrix}$$

$$\Rightarrow \quad \begin{bmatrix} B & S \end{bmatrix} = M = \begin{bmatrix} \vec{m}_1 & \cdots & \vec{m}_m \end{bmatrix}, \quad \mathbf{m} = \begin{bmatrix} \mathbf{b} \\ \mathbf{s} \end{bmatrix} = \text{vec}(\begin{bmatrix} B & S \end{bmatrix}).$$
(2b)

It is also useful to define a vector of member <u>lengths</u> ℓ , including a vector of bar lengths ℓ^b and a vector of string lengths ℓ^s , as well as a vector of normalized member <u>directions</u> \mathbf{d} , including a vector of normalized bar directions \mathbf{d}^b and a vector of normalized string directions \mathbf{d}^s , such that

$$\ell_{k} = \|\vec{m}_{k}\|, \qquad \ell_{i}^{b} = \|\vec{b}_{i}\|, \qquad \ell_{j}^{s} = \|\vec{s}_{j}\|, \qquad \ell = \begin{bmatrix} \boldsymbol{\ell}^{b} \\ \boldsymbol{\ell}^{s} \end{bmatrix},$$

$$\vec{d}_{k} = \vec{m}_{k}/\ell_{k}, \qquad \vec{d}_{i}^{b} = \vec{b}_{i}/\ell_{i}^{b}, \qquad \vec{d}_{j}^{s} = \vec{s}_{j}/\ell_{j}^{s}, \qquad \mathbf{d} = \begin{bmatrix} \mathbf{d}^{b} \\ \mathbf{d}^{s} \end{bmatrix} = \text{vec}(D),$$

$$D = \begin{bmatrix} \vec{d}_{1} & \cdots & \vec{d}_{m} \end{bmatrix} = \begin{bmatrix} D^{b} & D^{s} \end{bmatrix}, \quad D^{b} = \begin{bmatrix} \vec{d}_{1}^{b} & \cdots & \vec{d}_{b}^{b} \end{bmatrix}, \quad D^{s} = \begin{bmatrix} \vec{d}_{1}^{s} & \cdots & \vec{d}_{s}^{s} \end{bmatrix};$$

$$(2c)$$

note that $\|\vec{d}_k(t)\| = 1$ for all t. Following [16], the connectivity of a structure, relating the n nodes N in (2a) to the m members M in (2b), is described easily via its <u>connectivity matrix</u> C, defined and partitioned such that

$$M = N C^T$$
, $C = \begin{bmatrix} C_Q & C_P \end{bmatrix} = \begin{bmatrix} C_B \\ C_S \end{bmatrix} \Rightarrow \begin{bmatrix} B & S \end{bmatrix} = \begin{bmatrix} Q & P \end{bmatrix} \begin{bmatrix} C_Q^T \\ C_P^T \end{bmatrix} = \begin{bmatrix} Q & P \end{bmatrix} \begin{bmatrix} C_B & C_S^T \end{bmatrix}$, (2d)

where, denoting \mathbf{e}_j as the vector in the j'th column of the identity matrix, each column of C^T is given by $(\mathbf{e}_{k,1} - \mathbf{e}_{k,2})$, indicating the two nodes $\vec{n}_{k,1}$ and $\vec{n}_{k,2}$ that member \vec{m}_k connects, with one entry equal to 1, one entry equal to -1, and all other entries equal to zero; for the example structure illustrated in Figure 2, the first column of C^T is $\begin{pmatrix} -1 & 1 & 0 & \dots & 0 \end{pmatrix}^T$. Consider also external forces $\{\vec{u}_1, \dots, \vec{u}_q\}$, including the effects of the weight or buoyancy of the bars themselves, applied to each of the q free nodes, and reaction forces $\{\vec{v}_1, \dots, \vec{v}_p\}$ at each of the p fixed nodes, and similarly denote

$$U = \begin{bmatrix} \vec{u}_1 & \cdots & \vec{u}_q \end{bmatrix}, \quad \mathbf{u} = \text{vec}(U), \quad V = \begin{bmatrix} \vec{v}_1 & \cdots & \vec{v}_p \end{bmatrix}, \quad \mathbf{v} = \text{vec}(V), \quad W = \begin{bmatrix} U & V \end{bmatrix}.$$

⁵All vectors in \mathbb{R}^d are denoted with an arrow (e.g., $\vec{q_i}$). All other vectors, and quaternions, are denoted in bold (e.g., \mathbf{q}).

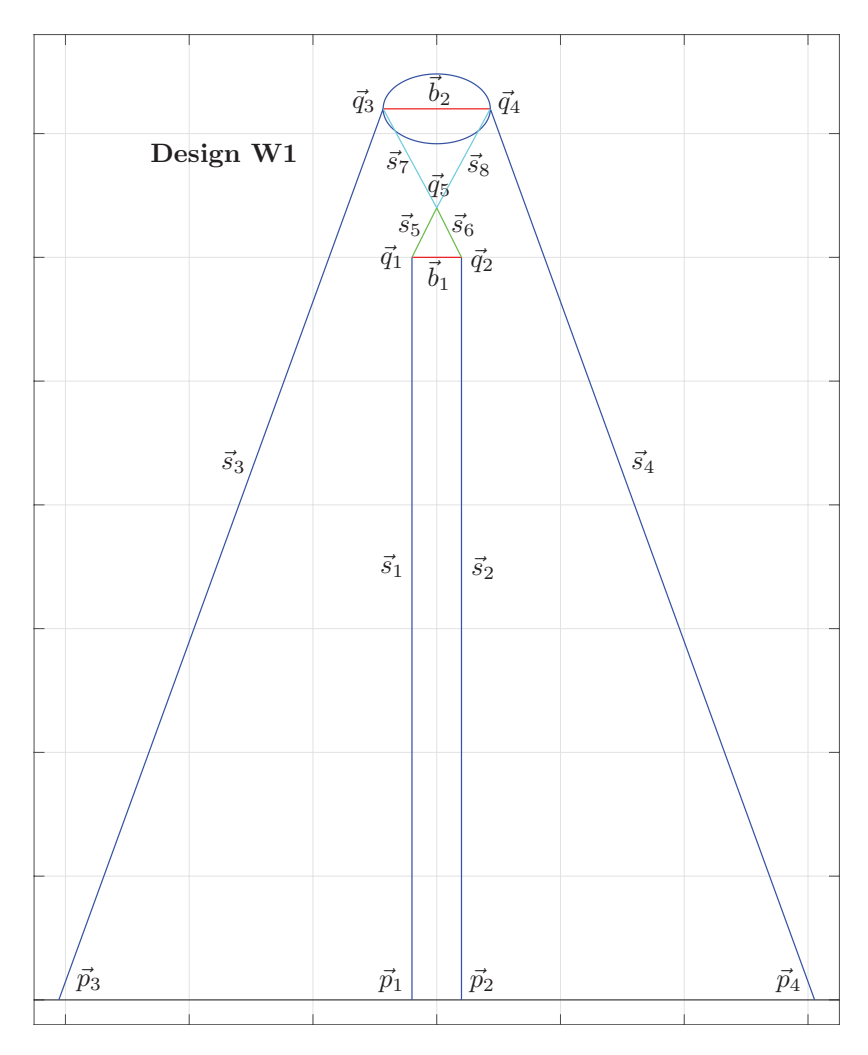


Figure 2: Initial (wobbly) 2D balloon rigging, Design W1, indicating the notation used in the analysis. The (heavy) payload is represented as bar \vec{b}_1 , with (effectively, massless) strings (a.k.a. tethers) \vec{s}_1 and \vec{s}_2 , attached at free nodes \vec{q}_1 and \vec{q}_2 (at the ends of this bar) connecting to ground points \vec{p}_1 and \vec{p}_2 . The (buoyant) balloon is represented as bar \vec{b}_2 , with strings \vec{s}_3 and \vec{s}_4 attached at the free nodes \vec{q}_3 and \vec{q}_4 and connecting to ground points \vec{p}_3 and \vec{p}_4 . The convergence point \vec{q}_5 , another free node, is attached to the nodal points on the payload, \vec{q}_1 and \vec{q}_2 , via tethers \vec{s}_5 and \vec{s}_6 . The convergence point \vec{q}_5 is also attached to the nodal points on the balloon, \vec{q}_3 and \vec{q}_4 , via a single tether, \vec{s}_7 - \vec{s}_8 , routed through a pulley at \vec{q}_5 , thereby equalizing the tension on these two strings and effectively isolating the pitching of the balloon \vec{b}_2 from the orientation of the payload \vec{b}_1 .

Internally, denote⁶ by $(\vec{d}_k x_k)$ and $-(\vec{d}_k x_k)$ the forces that member \vec{m}_k applies at nodes $\vec{n}_{k,2}$ and $\vec{n}_{k,1}$, respectively, where x_k denotes the tension force (if positive) or compression force (if negative) in member \vec{m}_k . Thus, the internal member forces may be written

$$DX = \begin{bmatrix} D^{b} & D^{s} \end{bmatrix} \begin{bmatrix} X^{b} & 0 \\ 0 & X^{s} \end{bmatrix} = \begin{bmatrix} D^{b} X^{b} & D^{s} X^{s} \end{bmatrix},$$
where $X = \operatorname{diag}(\mathbf{x}), \quad \mathbf{x} = \begin{bmatrix} \mathbf{x}^{b} \\ \mathbf{x}^{s} \end{bmatrix}, \quad X^{b} = \operatorname{diag}(\mathbf{x}^{b}), \quad X^{s} = \operatorname{diag}(\mathbf{x}^{s}).$ (3a)

$$DX = M\Sigma = \begin{bmatrix} B & S \end{bmatrix} \begin{bmatrix} -\Lambda & 0 \\ 0 & \Gamma \end{bmatrix} = \begin{bmatrix} -B\Lambda & S\Gamma \end{bmatrix} \text{ where } \Sigma = \operatorname{diag}(\sigma_1, \dots, \sigma_m), \quad \Lambda = \operatorname{diag}(\lambda_1, \dots, \lambda_b), \quad \Gamma = \operatorname{diag}(\gamma_1, \dots, \gamma_s).$$

⁶Note that [16] defines and solves for the force density $\sigma_k = x_k/\ell_k$ in each member, rather than solving for the forces x_k themselves (where, again positive σ_k denotes tension and negative σ_k denotes compression). They further denote the force density in string \vec{s}_j by γ_j (with, again, $\gamma_j > 0$ denoting tension), and the force density in bar \vec{b}_i by λ_i (with, in contrast, $\lambda_i > 0$ denoting compression). Using that (slightly more complicated) notation, the present derivation is expressed by applying the relations

It is assumed that bars can carry compressive or tensile forces, but strings can only carry tensile forces, and thus $x_j^s \geq 0$ for $j = 1, \ldots, s$. Following [16], the cumulative force \vec{f}_k at each node \vec{n}_k , due to the sum of all of the internal forces applied by each connected member \vec{m}_j (that is, due to the compression and tension forces of all the bars and strings), is then given simply by applying the connectivity matrix C to the above expression such that

$$\begin{bmatrix} \vec{f}_1 & \cdots & \vec{f}_n \end{bmatrix} = F = -DXC, \tag{3b}$$

with the minus sign because positive x_k denotes tension forces in the member direction $\vec{d_k}$. Static equilibrium is reached when sum of the internal forces at each node, F, is in balance with (that is, equal and opposite to) the external forces W at each node such that

$$F = -DXC = -W \implies DXC = \begin{bmatrix} U & V \end{bmatrix}$$
.

For any tensegrity structure with b bars B and s strings S connecting q free nodes Q and p fixed nodes P via the connectivity matrix C, as related in (2d), with external forces U applied at each free node, static equilibrium thus gives a linear system of equations in the m unknown forces $\{x_1, \ldots, x_m\}$ and the p unknown reaction forces V. As discussed further in §3.1.2, this linear system of equations may have $0, 1, \text{ or } \infty$ solutions, depending on the setup of the problem. The problem of determining the static equilibrium may be simplified by leveraging the partitioning $C = \begin{bmatrix} C_Q & C_P \end{bmatrix}$, and first solving for the forces at static equilibrium via

$$DXC_Q = U. (4a)$$

These conditions of static equilibrium, which are linear in the unknown member forces x_k , may easily be rewritten⁷ in terms of the vector \mathbf{x} in the standard matrix/vector form

$$A_{\rm se}\mathbf{x} = \mathbf{u} \tag{4b}$$

and solved, after which the reaction forces $\mathbf{v} = \text{vec}(V)$ may be computed directly via $V = DXC_P$.

3.1.1 Brief review of the Singular Value Decomposition (SVD)

Consider for a moment an arbitrary $\hat{m} \times \hat{n}$ matrix \hat{A} . It will be useful in the three subsections that follow to refer to the components of the block decomposition of the SVD, which may be defined as follows:

$$\hat{A}_{\hat{m}\times\hat{n}} = U_{\hat{m}\times\hat{m}} \, \Sigma_{\hat{m}\times\hat{n}} \, V_{\hat{n}\times\hat{n}}^H = \begin{bmatrix} \underline{U}_{\,\hat{m}\times r} & \overline{U}_{\,\hat{m}\times(\hat{m}-r)} \end{bmatrix} \begin{bmatrix} \underline{\Sigma}_{\,r\times r} & 0 \\ 0 & 0 \end{bmatrix} \begin{bmatrix} \underline{V}_{\,\hat{n}\times r} & \overline{V}_{\,\hat{n}\times(\hat{n}-r)} \end{bmatrix}^H,$$

where $\underline{\Sigma}$ is diagonal with real, non-negative elements σ_i on the main diagonal, arranged in descending order, U and V are unitary, and r is the \underline{rank} of the matrix A. Note that $\hat{A} = \underline{U\Sigma V}$. Much can be said about the matrix \hat{A} based on this decomposition. For the present purposes, recall simply that, for any $\hat{m} \times \hat{n}$ matrix \hat{A} ,

- (i) r is both the number of independent rows of \hat{A} and the number of independent columns of \hat{A} ,
- (ii) the columns of \hat{A} are spanned by the r orthogonal columns of \underline{U} ,
- (iii) the rows of \hat{A} are spanned by the r orthogonal rows of V^H ,
- (iv) the nullspace of \hat{A} (the space of all \mathbf{x} such that $\hat{A}\mathbf{x}=0$) is spanned by the $\hat{n}-r$ orthogonal columns of \overline{V} ,
- (v) the left nullspace of \hat{A} (the space of all \mathbf{y} such that $\hat{A}\mathbf{x} \neq \mathbf{y}$ for any \mathbf{x}) is spanned by the $\hat{m} r$ orthogonal columns of \overline{U} , and
- (vi) using the Moore-Penrose pseudoinverse $\hat{A}^+ = \underline{V}\underline{\Sigma}^{-1}\underline{U}^H$, the least-squares solution to $\hat{A}\mathbf{x} = \mathbf{b} + \boldsymbol{\epsilon}$, minimizing the norm of both $\boldsymbol{\epsilon}$ and \mathbf{x} , is $\mathbf{x} = \hat{A}^+\mathbf{b}$.

3.1.2 SVD analysis of the conditions of static equilibrium

The linear system of equations (4b) governing the member forces \mathbf{x} at static equilibrium of a proposed tensegrity structure may have 0, 1, or an infinite number of solutions. Stated differently, performing an SVD of the $\hat{m} \times \hat{n}$ matrix A_{se} , with $\hat{m} = dq$ and $\hat{n} = b + s$ (where d is the dimension of the problem considered, q is the number of free nodes, b is the number of bars, and s is the number of strings), the problem in (4b) is said to be:

(a) potentially inconsistent if $r < \hat{m}$, and thus $A_{\rm se}$ has some rows which are linearly dependent on the other rows [in this case, (4b) will either have 0 solutions or at least one solution, depending upon whether or not the external force vector \mathbf{u} is spanned by the columns of \underline{U}], and/or

⁷This task is conveniently handled symbolically in software, e.g. using equationsToMatrix in Matlab or sympy.expand in Python.

- (b) underdetermined if $r < \hat{n}$, and thus there are fewer independent equations than there are unknowns [in this case, if (4b) has one solution \mathbf{x} , then \mathbf{x} plus any linear combination of the $\overline{n} = \hat{n} r$ columns of \overline{V} is also a solution]. The equations of static equilibrium (4b) may thus be:
 - potentially inconsistent only $(\hat{m} > r = \hat{n})$, with 0 or 1 solution depending on **u**,
 - underdetermined only $(\hat{n} > r = \hat{m})$, with ∞ solutions,
 - both potentially inconsistent and underdetermined $(\hat{n} > r, \hat{m} > r)$, with 0 or ∞ solutions depending on **u**, or
- neither potentially inconsistent nor underdetermined $(\hat{n} = \hat{m} = r)$, with exactly 1 solution (this condition is called *static determinance*).

A tensegrity structure together with a nominal loading profile \mathbf{u}_0 will be called realizable if at least one solution to (4b) exists with all strings in tension for this nominal loading profile; note in particular that, even if (4b) is statically determinant, the corresponding tensegrity structure may not be realizable for this nominal loading profile if the corresponding force distribution \mathbf{x} does not have all strings in tension.

3.1.3 Elimination of infinitesimal modes from a (potentially inconsistent) tensegrity structure

If A_{se} is potentially inconsistent, with r < dq, then a corresponding tensegrity configuration with a realizable equilibrium for the nominal loading \mathbf{u}_0 has infinitesimal mechanisms associated with zero deformation energy. Such a configuration can be either unstable or soft. The first case (instability) is, clearly, catastrophic, with small disturbances acting on the structure leading rapidly to failure—visualize two opposing bars, under compression, meeting at a node (i.e., a ball joint) where external disturbance forces may be applied, with no strings attached to stabilize.

The second case (soft or "wobbly" modes), though not catastrophic, is also a highly undesirable feature for a tensegrity structure—visualize two opposing strings, under tension, meeting at a node where external forces may be applied. In this case, assuming all bars are rigid and strings non-stretchable, there are no finite force densities in the members that can sustain a range of disturbances on the nodes (specifically, any disturbances \mathbf{u} generated with components in the directions of the columns of \overline{U}) for this free node configuration \mathbf{q} . However, assuming (much more realistically) that the strings are somewhat elastic (and, again, that the system is realizable for the nominal loading), a significant deformation of the free node configuration vector \mathbf{q} (computed using the techniques of §3.2) may well lead to a deformed configuration that can sustain the problematic disturbance profile. Unfortunately, a different disturbance profile will generally lead to a different deformation of the structure, so this approach generally leads to a rather "wobbly" structure in the presence of unsteady external loads. Soft modes are thus also generally undesirable in a tensegrity structure, as they easily lead to relatively large deflections in response to small disturbances.

Fortunately, as discussed further in [11], the condition of potential inconsistency in (4b), with r < dq (and, the corresponding presence of unstable or soft modes), can often be removed entirely from a tensegrity structure with a given configuration of bars simply by judiciously adding more strings, thereby increasing r if the new strings are well positioned, as seen in the examples provided in §4.

3.1.4 Static tensioning of an (underdetermined) pretensionable tensegrity structure

If $A_{\rm se}$ is underdetermined, with r < b + s, then there are fewer independent equations than unknowns in (4b). This situation generally admits a certain control authority over the force distribution in the members, which can be useful if leveraged correctly. It is noted that most structures considered in the framework of tensegrity systems are, in fact, underdetermined. Further, most underdetermined tensegrity structures, with the notable exception of those proposed in this paper, are pretensionable, with a range of realizable force density distributions in the members (that is, with all strings in tension) possible even for zero nominal loading, $\mathbf{u}_0 = 0$. [The special case of underdetermined tensegrity structures that are not pretensionable, but still tensionable under load (meaning that there is a range of realizable force density distributions in the members, with all strings in tension, for some nonzero nominal external load, $\mathbf{u}_0 \neq 0$), is discussed further in §3.1.5.]

In the pretensionable setting, the question remains of how to adjust the remaining degrees of freedom in the structure such that all strings remain taut as time-varying nominal loads plus disturbances, $\mathbf{u}(t)$, are applied to the system, with the tensions greater than or equal to some minimum level $\tau_{\min} > 0$ in all strings to assure that none go slack, while the tensions in all strings in the structure also do not get too large, thereby risking failure. One convenient approach to address this problem is by framing it as a simple Linear Program (LP), as discussed below. [This approach is modified slightly in §3.1.5 for the case of underdetermined tensegrity structures that are not pretensionable, but are still tensionable under load.]

We start by assuming (that is, idealizing) that the strings are nonstretchable, and rewrite the equations of static equilibrium of a pretensionable tensegrity structure, $A_{se}\mathbf{x} = \mathbf{u}$, as

$$A_{\rm se}(\mathbf{x} + \boldsymbol{\delta}) = \mathbf{u}.$$

If $A_{\rm se}$ is underdetermined and the strings are idealized as nonstretchable, the distribution of (compression and tension) forces in the members, \mathbf{x} , may be replaced by $(\mathbf{x} + \boldsymbol{\delta})$ at any instant, where $\boldsymbol{\delta} = \overline{V}\mathbf{c}$ is any linear combination of the columns of \overline{V} (the vectors in the nullspace of $A_{\rm se}$), without affecting the static equilibrium itself. Assume we are starting from some static equilibrium condition $A_{\rm se}\mathbf{x} = \mathbf{u}$ for some (unknown) external loading $\mathbf{u}(t)$, and denote $\widetilde{\mathbf{x}}$ as the subset of the tensions in the \widetilde{m} measurable strings (i.e., those for which we can actually measure their tension⁸), $\widetilde{\boldsymbol{\delta}}$ as the corresponding elements of $\boldsymbol{\delta}$, and \widetilde{V} as the corresponding rows of \overline{V} . To assure, with some margin for error, that none of these \widetilde{m} strings go slack while not disrupting the static equilibrium achieved by the structure, we seek at any given timestep to update \mathbf{x} with $\boldsymbol{\delta}$ while respecting the \widetilde{m} conditions (written here in vector form) that

$$\widetilde{\mathbf{x}} + \widetilde{\boldsymbol{\delta}} \ge \tau_{\min} \mathbf{1}$$
 where $\widetilde{\boldsymbol{\delta}} = \widetilde{\overline{V}} \mathbf{c} \Rightarrow -\widetilde{\overline{V}} \mathbf{c} \le \widetilde{\mathbf{x}} - \tau_{\min} \mathbf{1}$ (5a)

for some (pre-selected) positive minimum tension τ_{\min} , where **1** is a vector with each element unity, and a vector inequality $\mathbf{a} \leq \mathbf{b}$ denotes element-wise inequality, $a_i \leq b_i$ for all i. We generally want to select the coefficient vector \mathbf{c} to achieve (5a) without letting any of the \widetilde{m} measurable tensions get too large. One convenient way of achieving this is to minimize a weighted one-norm of the value of $\widetilde{\mathbf{x}}$ after it is incremented by $\widetilde{\boldsymbol{\delta}}$; i.e., assuming \mathbf{x} is realizable (with no slack strings, so that $\widetilde{x}_m > 0$ for all of the \widetilde{m} measurable strings, and thus $C_0 = \mathbf{w}^T \widetilde{\mathbf{x}} > 0$), to solve

$$\underset{\mathbf{c}}{\operatorname{argmin}} \mathbf{w}^{T} (\widetilde{\mathbf{x}} + \widetilde{\overline{V}} \mathbf{c}) = C_{0} - \underset{\mathbf{c}}{\operatorname{argmax}} \widetilde{\mathbf{w}}^{T} \mathbf{c} \quad \text{where} \quad \widetilde{\mathbf{w}} = -(\widetilde{\overline{V}})^{T} \mathbf{w}$$
 (5b)

subject to (5a) [thus assuring that all components of $\tilde{\mathbf{x}} + \tilde{\boldsymbol{\delta}}$ are positive], where $\mathbf{w} > 0$. We can nominally take the weighting vector $\mathbf{w} = \mathbf{1}$; it may be useful⁹, however, to increase the weights somewhat on those measurable strings that, before the update (that is, as indicated in $\tilde{\mathbf{x}}$), are closest to breaking.

The problem formulated in (5a)-(5b) is easily rewritten and solved¹⁰ as a standard linear program (LP),

$$\overline{\mathbf{c}} = \underset{\overline{\mathbf{c}}}{\operatorname{argmax}} \overline{\mathbf{w}}^T \overline{\mathbf{c}} \quad \text{subject to} \quad \overline{A} \overline{\mathbf{c}} \le \overline{\mathbf{b}} \quad \text{and} \quad \overline{\mathbf{c}} \ge 0,$$
 (6a)

simply by decomposing $\mathbf{c} = \mathbf{c}^+ - \mathbf{c}^-$ where $\mathbf{c}^+ \geq 0$ and $\mathbf{c}^- \geq 0$, and defining $\overline{\mathbf{w}}$, $\overline{\mathbf{c}}$, \overline{A} , and $\overline{\mathbf{b}}$ as follows:

$$\overline{\mathbf{w}} = \begin{bmatrix} \widetilde{\mathbf{w}} \\ -\widetilde{\mathbf{w}} \end{bmatrix}, \quad \overline{\mathbf{c}} = \begin{bmatrix} \mathbf{c}^{+} \\ \mathbf{c}^{-} \end{bmatrix}, \quad \overline{A} = \begin{bmatrix} -\widetilde{V} & \widetilde{V} \end{bmatrix}, \quad \overline{\mathbf{b}} = \widetilde{\mathbf{x}} - \tau_{\min} \mathbf{1}.$$
 (6b)

At any timestep in the application of this approach, once the LP in (6) is solved¹¹ for $\overline{\mathbf{c}}$, the tensions in the *tensionable strings* (a subset of the measurable strings with winches at one end) are reset to their corresponding updated values, as evident in the corresponding element of $\mathbf{x} + \boldsymbol{\delta} = \mathbf{x} + \overline{V}\mathbf{c}$, and (assuming nonstretchable strings) the rest of the tensions in the structure will, essentially immediately (as all bars have some inertia), respond accordingly to maintain the structure at static equilibrium, while including the specified components \mathbf{c} of the nullspace vectors (the columns of \overline{V}) into the new force distribution $\mathbf{x}_{\text{new}} = \mathbf{x} + \overline{V}\mathbf{c}$ such that the minimum tensions in the measurable strings is τ_{min} , while simultaneously minimizing a weighted one-norm of the measurable string tensions, as specified in (5b).

Relaxing the idealization of nonstretchable strings, but adding the assumption that the external forcing $\mathbf{u}(t)$ varies only slowly in time as compared with the time constants of the modes of vibration of the resulting pretensioned structure, the updates to the tensions in the strings computed via this approach at each timestep may simply be passed through a suitable low-pass filter, in order to minimize the excitation of any structural vibration modes following this tensioning approach. If the external forcing $\mathbf{u}(t)$ varies too quickly for such an approach to be effective, a control approach based on a full analysis of the dynamics of the tensegrity structure (see §3.2) must be used instead, which involves significantly more finesse in the formulation and solution of the control problem at hand.

10

⁸Ideally, this includes all of the strings, or at least all of the strings which we are concerned about either going slack or breaking, upon analysis of the structure under the anticipated loading conditions; see §4.2.2-4.2.3 for examples. The number of strings \widetilde{m} in $\widetilde{\mathbf{x}}$ should be at least as large as the number of columns of \overline{V} for the method described to be solvable.

⁹Other ways of posing the problem of not allowing any of the (measurable) string tensions in $\tilde{\mathbf{x}}$ to get too large are possible. For example, if a single string material and diameter (and, thus, strength) is used everywhere, it might be preferred to minimize the infinity norm of $\tilde{\mathbf{x}}$. Formally, it is sometimes said that, in low dimensions, all norms are "equivalent", meaning in this case that the one norm bounds the infinity norm from both below and above, and vice-versa, i.e., $\|\tilde{\mathbf{x}}\|_1/\tilde{m} \leq \|\tilde{\mathbf{x}}\|_1 \leq \tilde{m} \|\tilde{\mathbf{x}}\|_{\infty}$; note, however, that these bounds become increasingly loose as the dimension \tilde{m} of the vector $\tilde{\mathbf{x}}$ is increased. Adjusting the weights in the weighted one-norm used here shifts the emphasis in the minimization problem (5b) to those directions that matter most, thus providing a solution using the one-norm that is in a sense closer to that provided using the infinity norm, while retaining the convenient structure of an LP.

 $^{^{10}}$ There are dozens of algorithms and efficient software libraries available to solve LPs, including linprog in Matlab and PuLP in Python. 11 Note that this can be done remarkably quickly, even for relatively large \widetilde{m} and even on a quite modest single-board computer.

3.1.5 Static tensioning of an (underdetermined) tensegrity structure that is tensionable under load

The tensegrity structures considered in this paper are not pretensionable; however, once the nominal load (that is, the buoyancy of the balloon and the weight of the payload) is applied, if r < b + s, there will be one or more degrees of freedom in the set of realizable solutions (with all strings in tension). These extra degrees of freedom may be set following the simple LP-based approach described in §3.1.4. However, it may well be useful to modify this approach slightly for this special case of tensegrity structures that are only tensionable under load. In such systems, only so much tension may be applied in any given string before one of the other stings goes slack (note that this is not the case in pretensionable structures); the primary concern in such systems is thus not really breaking a string, but in fact simply keeping all of the strings under tension as disturbances are applied.

It is thus desireable in this setting to change the objective in the LP discussed in §3.1.4 to the maximization of τ_{\min} itself, thereby in some respects maximizing the "margin" of additional disturbances that the structure can endure before one of the strings goes slack. Noting that the LP discussed previously is linear in τ_{\min} , this can be accomplished in the setting of (6a) simply by redefining $\overline{\mathbf{w}}$, $\overline{\mathbf{c}}$, \overline{A} , and $\overline{\mathbf{b}}$ as follows:

$$\overline{\mathbf{w}} = \begin{bmatrix} 0 \\ 0 \\ 1 \end{bmatrix}, \quad \overline{\mathbf{c}} = \begin{bmatrix} \mathbf{c}^+ \\ \mathbf{c}^- \\ \tau_{\min} \end{bmatrix}, \quad \overline{A} = \begin{bmatrix} -\widetilde{V} & \widetilde{V} & \mathbf{1} \end{bmatrix}, \quad \overline{\mathbf{b}} = \widetilde{\mathbf{x}}.$$
 (6c)

3.1.6 Open and closed kinematic chains

The analysis of the static equilibrium of a tensegrity structure lumps all forces (including those from the weight or buoyancy of the bars) at the nodes, and effectively treats the bars and strings in the same manner, the only significant difference being that strings are not allowed to provide compressive force. Indeed, which members of a tensegrity structure are bars, and which are stings, does not actually need to be decided upon until after the initial static equilibrium analysis is complete. In many tensionable tensegrity systems, in fact, all bars can be replaced by strings, and strings by bars, and a different tensioning solution again results in a realizable tensegrity structure.

In particular, the analysis of the static equilibrium of tensegrity structures is not complicated by cases in which bars directly attach to other bars, and/or to fixed points. This is in contrast with the analysis of the *dynamics* of tensegrity structures, in which Newton's laws for the time evolution of the position and orientation of the bars are solved, with the strings that interconnect the bars simply providing forces at the nodal points on the bars to which these strings attach, in the directions of the strings themselves and with magnitude proportional to the amount that these strings are stretched from their rest length. In such a setting, *constraints* on the time evolution of the position and orientation of the bars need to be applied if bars are initially attached to fixed nodes, in order to keep them so attached, and/or if bars are initially connected to other bars (a structure called a *kinematic chain*), in order to keep them so connected; such constraints on a time evolution can substantially complicate a numerical simulation code.

In the case of *open* kinematic chains (like robot manipulator arms), there are no closed loops; that is, at least one end of any chain of connected bars in the structure terminates with a free node. In this situation, a simple change of variables suffices to recast the constrained evolution of the position and orientation of the bars into an unconstrained time evolution in the modified variables. For example, imagine a kinematic chain that begins at a fixed node and ends at a free node. The bar that is connected to the fixed node is described by its (fixed) length together with a direction vector from the fixed node, the second bar in the chain is described by its length together with a direction vector from the end of the first bar, etc.; once Newton's laws for the time evolution of such a system are recast into these modified configuration variables, the (otherwise, difficult) constraints reflecting the connectivity of the kinematic chain(s) are then simply implicit to the configuration representation itself.

In the case of closed kinematic chains (like 4-bar linkages), however, the constraints inherent to the connections in the chain can not be eliminated with a simple change of variables; this case is generally much more difficult to simulate accurately. One approach to such a problem is to put a stretchable "fictitious string" of zero nominal length from the last node of the chain back to the fixed node (or, back to one of the previous free nodes in the chain) to which it connects. The stiffer this (critically damped) fictitious string is made, the more accurately the kinematic chain will be closed. Treating (via iteration at each timestep) the effect of the force caused by this fictitious string in the expression of Newton's equations for the time evolution of this system (in this constrained setting, a descriptor system) with the L-stable implicit part of an implicit/explicit (IMEX) time marching strategy for stiff systems [3] then allows the stiffness of the (critically damped) fictitious string to be taken as large (essentially infinite) without substantially limiting the timestep required for numerical stability of the simulation.

To simplify the discussion of tensegrity dynamics in §3.2, we will restrict our attention to the unconstrained setting in which no bars are attached to other bars, or to fixed points, as this simplified setting (once extended to account for embedded solid bodies) is entirely sufficient for the dynamic simulation of the structures proposed in §4.

3.2 Dynamics of unconstrained class 1 tensegrity systems with embedded solid bodies

Leveraging the precise notation defined in §3.1, and noting in particular the discussion of open and closed kinematic chains in §3.1.6, we now succinctly review the dynamics of 3D (i.e., d = 3) tensegrity systems with embedded solid bodies, generalizing the analysis presented in chapter 5 of [16], assuming that:

(a) each string is massless, exhibiting linear elastic behaviour when in tension and zero force when slack, such that each element of the vector $\mathbf{x}^{\mathbf{s}}$ of tension forces in the strings is now given by

$$x_{j}^{s} = \max\{0, \kappa_{j}(\|\vec{s}_{j}\| - \ell_{j}^{s,0})/\ell_{j}^{s,0})\}, \tag{7}$$

where $\ell_i^{\rm s,0}$ denotes the rest length of string \vec{s}_j [for the tether material mentioned in §1.3, $\kappa \approx 60/0.02 = 3000$],

- (b) each bar is rigid and slender, so that the degree of freedom (DOF) corresponding to rotation of each bar about its long axis may be neglected, with strings attached to the free nodes at each end,
- (c) each solid body has three nonzero principal moments of inertia $J_1 \ge J_2 \ge J_3 > 0$, so all three rotational DOF may be significant, with one or more free nodes affixed to the body at which strings may be attached,
- (d) the tensegrity system is, in the language of [16], unconstrained class 1, meaning that each bar (and, each embedded solid body) is only attached to strings (that is, not to other bars, nor to other solid bodies) and that the nodal points on each bar and on each solid body are free (not fixed), and
- (e) the connectivity of the members (strings, bars, and solid bodies) between the nodes (free and fixed) in the structure is prescribed by the connectivity matrix C, as denoted and defined in (2), with the columns of C^T corresponding to each solid body containing entries equal to 1 for each node (i.e., at each string attachment point) on the solid body.

Given these assumptions, the dynamics of the entire tensegrity structure is then described simply by writing Newton's laws for the time evolution of the linear and angular momentum of the bars and solid bodies, with the strings applying forces to the free nodes (at the ends of the bars, and at the attachment points on the solid bodies) at any instant as specified by (7). Rather than applying the conditions of static equilibrium, as done in §3.1 [see (4)], the (not necessarily balanced) forces at the nodes due to the tension and compression of the members, together with the external forces \mathbf{u} (including both disturbance forces as well as the weight or buoyancy of the bars and solid bodies) and reaction forces \mathbf{v} , apply net forces and torques which affect this time evolution, generally resulting, due to the elasticity of the strings, in both net deflections and possibly significant vibrations of the structure under time-varying loads. [Note that many tensegrity structures are only lightly damped before feedback control is applied.]

To proceed, define the bar location \vec{r}_k^b as the vector in \mathbb{R}^3 from the origin to the center of mass of bar b_k , the two ends nodes on which are denoted $\vec{n}_{k,1}^b$ and $\vec{n}_{k,2}^b$ (i.e., $\vec{b}_k = \vec{n}_{k,1}^b - \vec{n}_{k,2}^b$). Recall the definition of the bar length $\ell_k^b = ||\vec{b}_k||$ and the (normalized) bar direction $\vec{d}_k^b = \vec{b}_k/\ell_k^b$ which, noting assumption (b) above, uniquely defines the orientation of the bar. To simplify the discussion that follows, we also assume that the mass distribution of each bar is uniform, so that $\vec{r}_k^b = (\vec{n}_{k,1}^b + \vec{n}_{k,2}^b)/2$, and

$$\vec{n}_{k,1}^{\,b} = \vec{r}_k^{\,b} + (\ell_k^{\,b}/2)\,\vec{d}_k^{\,b}, \qquad \vec{n}_{k,2}^{\,b} = \vec{r}_k^{\,b} - (\ell_k^{\,b}/2)\,\vec{d}_k^{\,b}. \tag{8a}$$

[Note that this simplification is easily relaxed.] With these assumptions, the moment of inertia J_k^b of a (slender, uniform) bar \vec{b}_k with mass m_k , when rotated about its own center of mass and about an axis perpendicular to the bar direction vector \vec{d}_k^b , is $J_k^b = m_k \ell_k^2/12$. The ODEs governing the 5 DOF dynamics of a bar (that is, the time evolution of $\{\vec{r}_k^b, \vec{d}_k^b\}$ subject to $\|\vec{d}_k^b\| = 1$) is laid out in §3.2.1.

Define also the solid body location \vec{r}_k^{σ} as the vector in \mathbb{R}^3 from the origin to the center of mass of solid body σ_k with principal moments $J_{k,1}^{\sigma} \geq J_{k,2}^{\sigma} \geq J_{k,3}^{\sigma} > 0$, the a_k attachment nodes on which are defined in the (unrotated) principal coordinates of the body as $\vec{n}_{k,1}^{\sigma,B}, \ldots, \vec{n}_{k,a_k}^{\sigma,B}$, and are denoted in global coordinates as $\vec{n}_{k,1}^{\sigma}, \ldots, \vec{n}_{k,a_k}^{\sigma}$. The configuration of the solid body in the global frame is defined as a rotation and translation from a nominal configuration in the body frame B, in which the center of mass of the body is at the origin and the principal axes of the body are aligned with the $\{x, y, z\}$ axes, via a corresponding (4-component) unit quaternion \mathbf{d}_k^{σ} (reviewed in §3.2.2) such that

$$\vec{n}_{k,i}^{\sigma} = \vec{r}_k^{\sigma} + \mathbf{d}_k^{\sigma} \, \vec{n}_{k,i}^{\sigma,B} \left(\mathbf{d}_k^{\sigma} \right)^* \quad \text{for } i = 1, \dots, a_k.$$
(8b)

The ODEs governing the 6 DOF dynamics of a solid body (that is, the time evolution of $\{\vec{r}_k^{\sigma}, \mathbf{d}_k^{\sigma}\}$ subject to $\|\mathbf{d}_k^{\sigma}\| = 1$) is laid out in §3.2.2.

The dynamics of an entire unconstrained class 1 tensegrity system with embedded solid bodies is then given simply by interconneting its b bars (see §3.2.1), σ solid bodies (see §3.2.2), and p fixed nodes with s elastic strings, the tension of which is governed by (7), as summarized in §3.2.3.

3.2.1 5 DOF dynamics of a single bar

For notational convenience in this subsection only, which focuses exclusively on bar b_k , we drop the k subscript and b superscript on all variables. Given this, the linear momentum of the bar is simply $(m\,\dot{\vec{r}})$, and its angular momentum \vec{h} may be written as the product of the moment of inertia of the bar about its center, J, and the cross product of the normalized bar direction vector \vec{d} with its time derivative $\dot{\vec{d}}$, noting that $\|\vec{d}(t)\| = 1$ for all t:

$$\vec{h} = J \, \vec{d} \times \dot{\vec{d}} = J \, \widetilde{D} \, \dot{\vec{d}} \quad \text{where} \quad \widetilde{D} = \begin{pmatrix} 0 & -d_3 & d_2 \\ d_3 & 0 & -d_1 \\ -d_2 & d_1 & 0 \end{pmatrix}. \tag{9}$$

We are now in a position to write Newton's laws for the time evolution of the linear and angular momentum of the bar. The linear acceleration of the bar is, of course, governed simply by

$$m \ddot{\vec{r}} = \vec{f_1} + \vec{f_2} + \vec{u} \tag{10}$$

where $\vec{f_1}$ is the sum of all string forces at one end of the bar, $\vec{f_2}$ is the sum of all string forces at the other end of the bar, and \vec{u} includes all additional forces on the bar. Similarly, differentiating (9) and noting that $\vec{a} \times \vec{a} = 0$ for any vector \vec{a} , the angular acceleration of the bar is governed by

$$d\vec{h}/dt = \dot{\vec{h}} = J \ \vec{d} \times \ddot{\vec{d}} = J \ \widetilde{D} \ \ddot{\vec{d}} = \vec{\tau} = \vec{d} \times \vec{\phi} = \widetilde{D} \ \vec{\phi} \quad \text{where} \quad \vec{\phi} = \eta_1 \ \vec{f}_1 + \eta_2 \ \vec{f}_2 + \eta_3 \ \vec{u}, \tag{11}$$

where $\vec{\phi}$ (the generalized force driving the evolution equation for \vec{d}) is such that $\vec{\tau} = \vec{d} \times \vec{\phi}$, and thus $\vec{\phi}$ arises due to the forces applied at its ends, $\vec{f_1}$ and $\vec{f_2}$, acting via moment arms of $\eta_1 = \ell/2$ and $\eta_2 = -\ell/2$ respectively, as well as the sum of all additional forces acting on the bar, \vec{u} , acting via some cumulative third moment arm η_3 , the modeling of which is problem specific (often, $\eta_3 = 0$). We now apply the constraint that $||\vec{d}|| = 1$, and thus, via differentiation,

$$\|\vec{d}\|^2 = \vec{d}^T \vec{d} = 1 \quad \Rightarrow \quad \vec{d}^T \dot{\vec{d}} = 0 \quad \Rightarrow \quad \vec{d}^T \ddot{\vec{d}} + \|\dot{\vec{d}}\|^2 = 0.$$
 (12)

Note that \widetilde{D} is singular (in particular, $\widetilde{D} \vec{d} = 0$), and thus (11) alone is insufficient to define the evolution of \vec{d} . Thus, writing $J \widetilde{D} \dot{\vec{d}} = \vec{\tau}$ from (11) and $\vec{d}^T \dot{\vec{d}} + ||\dot{\vec{d}}||^2 = 0$ from (12) as a system of simultaneous equations gives

$$A_1 \ddot{\vec{d}} = \begin{bmatrix} \vec{\tau}/J \\ -\|\dot{\vec{d}}\|^2 \end{bmatrix} \quad \text{where} \quad A_1 = \begin{bmatrix} \tilde{D} \\ \vec{d}^T \end{bmatrix}. \tag{13}$$

This system of simultaneous equations may be simplified (again, following [16]) by first noting that

$$A_{1}^{T} A_{1} = \begin{bmatrix} \widetilde{D}^{T} & \vec{d} \end{bmatrix} \begin{bmatrix} \widetilde{D} \\ \vec{d}^{T} \end{bmatrix} = \begin{pmatrix} 0 & d_{3} & -d_{2} & d_{1} \\ -d_{3} & 0 & d_{1} & d_{2} \\ d_{2} & -d_{1} & 0 & d_{3} \end{pmatrix} \begin{pmatrix} 0 & -d_{3} & d_{2} \\ d_{3} & 0 & -d_{1} \\ -d_{2} & d_{1} & 0 \\ d_{1} & d_{2} & d_{3} \end{pmatrix} = \begin{pmatrix} \|\vec{d}\|^{2} & 0 & 0 \\ 0 & \|\vec{d}\|^{2} & 0 \\ 0 & 0 & \|\vec{d}\|^{2} \end{pmatrix} = \|\vec{d}\|^{2} I$$

$$\Rightarrow \widetilde{D}^{T} \widetilde{D} + \vec{d} \vec{d}^{T} = \|\vec{d}\|^{2} I. \tag{14a}$$

The columns of A_1 are seen to be orthogonal, each with norm $\|\vec{d}\|^2$. The matrix

$$A_1^+ = A_1^T / \|\vec{d}\|^2 = \left[\tilde{D}^T \quad \vec{d} \right] / \|\vec{d}\|^2$$
 (14b)

is thus the (unique) left inverse of the 4×3 matrix A_1 , and the unique solution of (13), noting (14), is

$$\vec{d} = A_1^+ \begin{bmatrix} \vec{\tau}/J \\ -\|\vec{d}\,\|^2 \end{bmatrix} = \begin{bmatrix} \widetilde{D}^T & \vec{d} \end{bmatrix} \begin{bmatrix} \vec{\tau}/J \\ -\|\vec{d}\,\|^2 \end{bmatrix} / \|\vec{d}\,\|^2 = \widetilde{D}^T \, \widetilde{D} \, \vec{\phi} / (J \, \|\vec{d}\,\|^2) - \vec{d} \, \|\vec{d}\,\|^2 / \|\vec{d}\,\|^2
\Rightarrow \quad \ddot{\vec{d}} = \{ I - \vec{d} \, \vec{d}^T / \|\vec{d}\,\|^2 \} \, (\eta_1 \, \vec{f}_1 + \eta_2 \, \vec{f}_2 + \eta_3 \, \vec{u}) / J - (\|\vec{d}\,\|/\|\vec{d}\,\|)^2 \vec{d} \,. \tag{15}$$

As an (equivalent) alternative to the second-order ODE in (15), one can instead march a pair of first-order ODEs when simulating the time evolution of the bar direction \vec{d} by writing $\widetilde{D} \, \dot{\vec{d}} = \vec{h}/J$ from (9) and $\vec{d}^T \dot{\vec{d}} = 0$ from (12) as a system of simultaneous equations, leveraging (14b) as before, and noting (11), thus giving

$$A_1 \vec{d} = \begin{bmatrix} \vec{h}/J \\ 0 \end{bmatrix} \quad \Rightarrow \quad \vec{d} = \begin{bmatrix} \widetilde{D}^T & \vec{d} \end{bmatrix} \begin{bmatrix} \vec{h}/J \\ 0 \end{bmatrix} / \|\vec{d}\|^2 \quad \Rightarrow \quad \vec{d} = \widetilde{D}^T \vec{h}/(J\|\vec{d}\|^2), \quad \dot{\vec{h}} = \widetilde{D} (\eta_1 \vec{f}_1 + \eta_2 \vec{f}_2 + \eta_3 \vec{u}). \quad (16)$$

Equations (10) and (15) [alternatively, the pair of first-order forms in (16)] thus give the ODEs governing the time evolution of the 5 DOF defining the configuration of the bar in 3D, as defined by $\{\vec{r}, \vec{d}\}$ and influenced by $\{\vec{f}_1, \vec{f}_2, \vec{u}\}$, which includes the forces due to the tensions of the strings attached to its two ends, \vec{f}_1 and \vec{f}_2 , as well as \vec{u} , which includes all additional forces on the bar (due to external disturbances and the weight or buoyancy of the bar itself). Note that this system evolves on the manifold $\|\vec{d}\| = 1$, which is enforced in (15) by incorporating $\vec{d}^T \vec{d} + \|\vec{d}\|^2 = 0$ from (12), and is enforced in (16) by incorporating $\vec{d}^T \vec{d} = 0$ from (12). Time marching errors can lead to $\|\vec{d}\|$ drifting away from unity during the numerical simulation of either form; occasionally renormalizing \vec{d} during such a simulation can easily correct for such errors. For further discussion and comparison of the numerical stability of these forms, see [10].

3.2.2 6 DOF dynamics of a single solid body

For notational convenience in this subsection only, which focuses exclusively on solid body σ_k , we drop the k subscript and σ superscript on all variables. As before, the linear acceleration of the solid body is governed simply by

$$m \, \ddot{\vec{r}} = \sum_{i=1}^{a} \vec{f_i} + \vec{u}$$
 (17)

where $\vec{f_i}$ is the force is due to all of the strings connected at each of the a attachment points on the solid body, and \vec{u} includes all additional forces on the solid body.

We now review the framework for the rotational dynamics of solid bodies leveraging quaternions¹². The *unit* quaternion $\mathbf{d} = d_0 + d_1 \mathbf{i} + d_2 \mathbf{j} + d_3 \mathbf{k}$ is taken to represent the rotation of any vector \vec{p}^B in the <u>Body</u> frame (e.g., to any specific point \vec{p}^B on the solid body) to the corresponding vector \vec{p} in the global frame, giving¹³

$$\vec{p} = \mathbf{d} \, \vec{p}^B \mathbf{d}^* = \begin{pmatrix} (d_0^2 + d_1^2 - d_2^2 - d_3^2) & 2(d_1 d_2 - d_0 d_3). & 2(d_1 d_3 + d_0 d_2) \\ 2(d_1 d_2 + d_0 d_3) & (d_0^2 - d_1^2 + d_2^2 - d_3^2) & 2(d_2 d_3 - d_0 d_1) \\ 2(d_1 d_3 - d_0 d_2) & 2(d_2 * d_3 + d_0 * d_1). & (d_0^2 - d_1^2 - d_2^2 + d_3^2) \end{pmatrix} \vec{p}^B,$$
(19)

where $\mathbf{d}^* = d_0 - d_1 \mathbf{i} - d_2 \mathbf{j} - d_3 \mathbf{k}$ denotes the conjugate of unit quaternion \mathbf{d} , with $\|\mathbf{d}\|^2 = \mathbf{d}^* \mathbf{d} = \mathbf{d} \mathbf{d}^* = d_0^2 + d_1^2 + d_2^2 + d_3^2 = 1$. Leveraging the constraint $\|\mathbf{d}\|^2 = 1$, it may be shown that

$$\dot{\mathbf{d}} = \vec{\omega} \, \mathbf{d}/2 = \mathbf{d} \, \vec{\omega}^B / 2 \tag{20}$$

where $\vec{\omega}^B$ is the *instantaneous rate of rotation* of the body in the body frame, and $\vec{\omega}$ is the corresponding representation of this instantanous rate of rotation in the global frame. It may also be shown that, in the body frame (rotating with the solid body, with inertial matrix J), Euler's equations of motion are

$$J\dot{\vec{\omega}}^B + \vec{\omega}^B \times (J\vec{\omega}^B) = \vec{\tau}^B, \tag{21a}$$

where $\vec{\tau}^B$ is the total torque applied to the body about each of its (body-fixed) coordinate axes; if these coordinate axes are aligned with the principal coordinate directions of the body, Euler's equations (21a) conveniently reduce to

$$J_1 \dot{\omega}_1^B + (J_3 - J_2) \omega_2^B \omega_3^B = \tau_1^B, \quad J_2 \dot{\omega}_2^B + (J_1 - J_3) \omega_3^B \omega_1^B = \tau_2^B, \quad J_3 \dot{\omega}_3^B + (J_2 - J_1) \omega_1^B \omega_2^B = \tau_3^B.$$
 (21b)

$$\mathbf{i}^2 = \mathbf{j}^2 = \mathbf{k}^2 = \mathbf{i}\mathbf{j}\mathbf{k} = -1 \quad \Rightarrow \quad \mathbf{i}\mathbf{j} = -\mathbf{j}\mathbf{i} = \mathbf{k}, \quad \mathbf{j}\mathbf{k} = -\mathbf{k}\mathbf{j} = \mathbf{i}, \quad \mathbf{k}\mathbf{i} = -\mathbf{i}\mathbf{k} = \mathbf{j}, \tag{18a}$$

the Hamilton product of two quaternions $\mathbf{p} = p_0 + p_1 \mathbf{i} + p_2 \mathbf{j} + p_3 \mathbf{k} = p_0 + \vec{p}$ and $\mathbf{q} = q_0 + q_1 \mathbf{i} + q_2 \mathbf{j} + q_3 \mathbf{k} = q_0 + \vec{q}$, where $\vec{p} = p_1 \mathbf{i} + p_2 \mathbf{j} + p_3 \mathbf{k}$ and $\vec{q} = q_1 \mathbf{i} + q_2 \mathbf{j} + q_3 \mathbf{k}$, treats \mathbf{i} , \mathbf{j} , and \mathbf{k} like noncommutative algebraic variables; applying (18a), this results in

$$\mathbf{r} = \mathbf{p} \, \mathbf{q} = r_0 + r_1 \mathbf{i} + r_2 \mathbf{j} + r_3 \mathbf{k} = (p_0 + \vec{p})(q_0 + \vec{q}) = (p_0 q_0 - \vec{p} \cdot \vec{q}) + (p_0 \vec{q} + q_0 \vec{p} + \vec{p} \times \vec{q}) \tag{18b}$$

$$\Rightarrow \begin{pmatrix} r_0 \\ r_1 \\ r_2 \\ r_3 \end{pmatrix} = \begin{pmatrix} p_0 & -p_1 & -p_2 & -p_3 \\ p_1 & p_0 & -p_3 & p_2 \\ p_2 & p_3 & p_0 & -p_1 \\ p_3 & -p_2 & p_1 & p_0 \end{pmatrix} \begin{pmatrix} q_0 \\ q_1 \\ q_2 \\ q_3 \end{pmatrix} = \begin{pmatrix} q_0 & -q_1 & -q_2 & -q_3 \\ q_1 & q_0 & q_3 & -q_2 \\ q_2 & -q_3 & q_0 & q_1 \\ q_3 & q_2 & -q_1 & q_0 \end{pmatrix} \begin{pmatrix} p_0 \\ p_1 \\ p_2 \\ p_3 \end{pmatrix}, \tag{18c}$$

where $\vec{p} \cdot \vec{q}$ and $\vec{p} \times \vec{q}$ denote 3D dot and cross products. Equations like (19) treat vectors in \mathbb{R}^3 like quaternions with zero real part. ¹³Writing $\mathbf{d} = e^{\vec{u} \phi} = e^{(u_1 \mathbf{i} + u_2 \mathbf{j} + u_3 \mathbf{k}) \phi} = \cos \phi + (u_1 \mathbf{i} + u_2 \mathbf{j} + u_3 \mathbf{k}) \sin \phi$ for $||\vec{u}|| = 1$, (19) gives a clockwise rotation of \vec{p}^B about the unit vector \vec{u} by an angle $\theta = 2\phi$.

¹²Based on Hamilton's 1843 construction

The torque $\vec{\tau}^B$, in turn, is related to the forces \vec{f}_i due to all of the strings connected at each of the $i=1,\ldots,a$ attachment points, as well as the additional forces on the solid body \vec{u} , as follows

$$\vec{\tau}^B = \sum_{i=1}^a \vec{n}_i^B \times \vec{f}_i^B + \vec{\eta}^B \times \vec{u}^B \quad \text{where} \quad \vec{f}_i^B = \mathbf{d}^* \vec{f}_i \mathbf{d}, \quad \vec{u}^B = \mathbf{d}^* \vec{u} \mathbf{d}$$
 (22a)

where, as mentioned previously, the a attachment nodes on the body are defined in the principal coordinates of the body as $\vec{n}_1^B, \dots, \vec{n}_a^B$, and the modeling of moment arm $\vec{\eta}^B$ is problem specific (often, $\vec{\eta}^B = 0$). Taking the time derivative of $\dot{\mathbf{d}} = \mathbf{d} \vec{\omega}^B/2$ from (20) and substituting (21a) and $\vec{\omega}^B = 2 \mathbf{d}^* \dot{\mathbf{d}}$ results in a nonlinear second-order equation for the time evolution of the unit quaternion \mathbf{d} :

$$\ddot{\mathbf{d}} = \left\{ \dot{\mathbf{d}} \,\vec{\omega}^B + \mathbf{d} \,\dot{\vec{\omega}}^B \right\} / 2 = \left\{ \dot{\mathbf{d}} \,\vec{\omega}^B + \mathbf{d} J^{-1} [\vec{\tau}^B - \vec{\omega}^B \times (J \,\vec{\omega}^B)] \right\} / 2$$

$$\Rightarrow \quad \ddot{\mathbf{d}} = \dot{\mathbf{d}} \,\mathbf{d}^* \,\dot{\mathbf{d}} + \mathbf{d} \,J^{-1} [\vec{\tau}^B - 4 \,\mathbf{d}^* \dot{\mathbf{d}} \times (J \,\mathbf{d}^* \dot{\mathbf{d}})] / 2. \tag{22b}$$

Note also the constraint that $\|\mathbf{d}\| = 1$, and thus, via differentiation,

$$\|\mathbf{d}\|^2 = \mathbf{d}^*\mathbf{d} = 1 \quad \Rightarrow \quad \mathbf{d}^*\dot{\mathbf{d}} + \dot{\mathbf{d}}^*\mathbf{d} = 2[\mathbf{d}^*\dot{\mathbf{d}}]_0 = 0 \quad \Rightarrow \quad \mathbf{d}^*\ddot{\mathbf{d}} + \ddot{\mathbf{d}}^*\mathbf{d} + 2\dot{\mathbf{d}}^*\dot{\mathbf{d}} = 0 \quad \Rightarrow \quad [\mathbf{d}^*\ddot{\mathbf{d}}]_0 = -\dot{\mathbf{d}}^*\dot{\mathbf{d}}, \tag{23}$$

where $[\mathbf{p}]_0$ denotes the real part of \mathbf{p} . Note that (22b) is consistent with this constraint, which is used implicitly in the writing of (20) upon which it is derived. This may be seen by defining $\mathbf{p} = \mathbf{d}^*\dot{\mathbf{d}}$ (note that, by (23), $[\mathbf{p}]_0 = 0$, and thus \mathbf{p} may, by footnote 12, be denoted by its vector part \vec{p}) and premultiplying (22b) by \mathbf{d}^* , leading to

$$\mathbf{d}^*\ddot{\mathbf{d}} = \mathbf{p}\,\mathbf{p} + \|\mathbf{d}\|^2 J^{-1}[\vec{\tau}^B - 4\,\vec{p} \times (J\,\vec{p})]/2;$$

by (18b), the first term on the RHS is the real part of $\mathbf{d}^*\ddot{\mathbf{d}}$, and the second term is the vector part of $\mathbf{d}^*\ddot{\mathbf{d}}$. Note in particular that this formula gives $[\mathbf{d}^*\ddot{\mathbf{d}}]_0 = \mathbf{p}\,\mathbf{p} = -\mathbf{p}^*\mathbf{p} = -\dot{\mathbf{d}}^*\mathbf{d}\,\mathbf{d}^*\dot{\mathbf{d}} = -\dot{\mathbf{d}}^*\dot{\mathbf{d}}$, as required by (23).

As an (equivalent) alternative to the second-order ODE in (22a)-(22b), one can instead march a pair of first-order ODEs when simulating the time evolution of the solid body orientation \mathbf{d} via $\dot{\mathbf{d}} = \mathbf{d} \vec{\omega}^B/2$ from (20), which is inherently consistent with $[\mathbf{d}^*\dot{\mathbf{d}}]_0 = 0$ from (23), in parallel with (21a) [or (21b), as appropriate].

Noting (22a), equations (17) and (22b) [alternatively, the pair of first-order forms (20) and (21a) or (21b)] thus give the ODEs governing the time evolution of the 6 DOF defining the configuration of the solid body in 3D, as defined by $\{\vec{r}, \mathbf{d}\}$ and influenced by $\{\vec{f}_1, \dots, \vec{f}_a, \vec{u}\}$, which includes the forces due to the tensions of the strings attached to each of its a attachments points, \vec{f}_1 to \vec{f}_a , as well as \vec{u} , which includes all additional forces on the solid body (due to external disturbances and the weight or buoyancy of the solid body itself). Note that this system evolves on the manifold $\|\mathbf{d}\| = 1$. Again, time marching errors can lead to $\|\mathbf{d}\|$ drifting away from unity during the numerical simulation of either form; occasionally renormalizing \mathbf{d} during such a simulation can correct for such errors. For further discussion, see [12, 15].

3.2.3 Dynamics of an entire tensegrity structure

The complete set of equations governing the dynamics [that is, the time evolution of the configuration vector $\mathbf{q}(t)$] of an entire elastic class 1 tensegrity system, with bars and solid bodies interconnected by elastic strings, in response to (nominal plus disturbance) time-varying loads $\mathbf{u}(t)$, may now be pieced together. This set of equations is given by the dynamic equations for the time evolution of the position and direction $\{\vec{r}_k^b, \vec{d}_k^b\}$ of each individual bar b_k , as given in (10) and (16) [using the pair of first-order forms for the bar direction]:

$$\ddot{\vec{r}}_k^b = (\vec{f}_{k,1}^b + \vec{f}_{k,2}^b + \vec{u}_k^b)/m_k^b, \tag{24a}$$

$$\dot{\vec{d}}_k^{\ b} = -\vec{d}_k^{\ b} \times \vec{h}_k^{\ b} / (J_k^{\ b} \| \vec{d}_k^{\ b} \|^2), \qquad \dot{\vec{h}}_k^{\ b} = \vec{d}_k^{\ b} \times \left(\eta_{k,1}^{\ b} \, \vec{f}_{k,1}^{\ b} + \eta_{k,2}^{\ b} \, \vec{f}_{k,2}^{\ b} + \eta_{k,3}^{\ b} \, \vec{u}_k^{\ b} \right), \tag{24b}$$

and time evolution of the position and orientation $\{\vec{r}_k^{\sigma}, \mathbf{d}_k^{\sigma}\}\$ of each individual solid body σ_k , as given in (17) and (20)-(21b)-(22a) [using the pair of first-order forms, in principal coordinates, for the solid body orientation]:

$$\ddot{\vec{r}}_k^{\sigma} = \left(\sum_{i=1}^a \vec{f}_{k,i}^{\sigma} + \vec{u}_k^{\sigma}\right) / m_k^{\sigma},\tag{24c}$$

$$\dot{\mathbf{d}}_{k}^{\sigma} = \mathbf{d}_{k}^{\sigma} \, \vec{\omega}_{k}^{\sigma,B} / 2, \qquad \dot{\vec{\omega}}_{k}^{\sigma,B} = \begin{pmatrix} [\tau_{k,1}^{\sigma,B} - (J_{k,3}^{\sigma} - J_{k,2}^{\sigma}) \, \omega_{k,2}^{\sigma,B} \, \omega_{k,3}^{\sigma,B}] / J_{k,1}^{\sigma} \\ [\tau_{k,2}^{\sigma,B} - (J_{k,1}^{\sigma} - J_{k,3}^{\sigma}) \, \omega_{k,3}^{\sigma,B} \, \omega_{k,1}^{\sigma,B}] / J_{k,2}^{\sigma} \\ [\tau_{k,2}^{\sigma,B} - (J_{k,2}^{\sigma} - J_{k,1}^{\sigma}) \, \omega_{k,3}^{\sigma,B} \, \omega_{k,2}^{\sigma,B}] / J_{k,3}^{\sigma} \end{pmatrix}, \tag{24d}$$

where
$$\vec{\tau}_k^{\sigma,B} = \sum_{i=1}^a \vec{n}_{k,i}^{\sigma,B} \times \left[(\vec{\mathbf{d}}_k^{\sigma})^* \vec{f}_{k,i}^{\sigma} \mathbf{d}_k^{\sigma} \right] + \vec{\eta}_k^{\sigma,B} \times \left[(\mathbf{d}_k^{\sigma})^* \vec{u}_k^{\sigma} \mathbf{d}_k^{\sigma} \right].$$
 (24e)

The dynamics of the bars are influenced by the forces $\vec{f}_{k,1}^b$ and $\vec{f}_{k,2}^b$ due to the tensions of the strings attached to the end nodes on each bar, $\vec{n}_{k,1}^b$ and $\vec{n}_{k,2}^b$, and \vec{u}_k^b , which includes all additional forces on each bar, and the dynamics of the solid bodies are influenced by the forces $\vec{f}_{k,1}^\sigma$ to \vec{f}_{k,a_k}^σ due to the tensions of the strings attached to each of the a_k attachment nodes on each solid body, $\vec{n}_{k,1}^\sigma$ to \vec{n}_{k,a_k}^σ , and \vec{u}_k^σ , which includes all additional forces on each solid body. To determine the forces from the strings, the locations of the end nodes on each bar, $\vec{n}_{k,1}^b$ and $\vec{n}_{k,2}^b$, are first related to the bar positions and directions, $\{\vec{r}_k^b, \vec{d}_k^b\}$, as in (8a), and the locations of the attachment nodes on the solid bodies, $\vec{n}_{k,1}^\sigma$ to \vec{n}_{k,a_k}^σ , are related to the solid body positions and orientations, $\{\vec{r}_k^\sigma, \mathbf{d}_k^\sigma\}$, as in (8b). Defining

$$\mathbf{q} = \begin{pmatrix} \vec{n}_{1,1}^b & \vec{n}_{1,2}^b & \dots & \vec{n}_{b,1}^b & \vec{n}_{b,2}^b & \vec{n}_{1,1}^\sigma & \dots & \vec{n}_{1,a_1}^\sigma & \dots & \vec{n}_{\sigma,1}^\sigma & \dots & \vec{n}_{\sigma,a_\sigma}^\sigma \end{pmatrix},$$

$$\hat{\mathbf{q}} = \begin{pmatrix} \vec{r}_1^b & \vec{d}_1^b & \dots & \vec{r}_b^b & \vec{d}_b^b & \vec{r}_1^\sigma & \mathbf{d}_1^\sigma & \dots & \vec{r}_\sigma^\sigma & \mathbf{d}_\sigma^\sigma \end{pmatrix},$$

and noting the two matrix forms for quaternion multiplication in (18c), the linear relations in (8a)-(8b) may easily be written in matrix form $\mathbf{q} = \Xi \, \widehat{\mathbf{q}}$, where $\Xi = \Xi_{3(2b+a_a+a_2+...+a_\sigma)\times d(6b+7\sigma)}$ is block diagonal. Finally, the forces due to the tensions in the strings can easily be determined from the locations of the free and fixed nodes, \mathbf{q} and \mathbf{p} , via the elasticity (stretch-to-tension) relationship (7), leveraging the connectivity relationship $S = \begin{bmatrix} Q & P \end{bmatrix} C_S^T$ defining the string vectors $\vec{s_j}$, the (normalized) direction of each of these strings, $\vec{d_j}^s = \vec{s_j}/\ell_j^s$, and the degree to which the length of each of these strings, $\ell_j^s = \|\vec{s_j}\|$, is stretched beyond its rest length $\ell_j^{s,0}$.

Again, time marching errors can lead to $\|\vec{d}_k^b\|$ and $\|\mathbf{d}_k^\sigma\|$ durifying away from unity during numerical simulations of these equations; occasionally renormalizing \vec{d}_k^b and \mathbf{d}_k^σ during such simulations can easily correct for such errors. Note also that the vector of (nominal plus disturbance) forces \mathbf{u} acting on the system in this dynamic formulation is, perhaps most naturally, modelled for each bar and solid body, not for each node [cf. the definition of \mathbf{u} in §3.1].

4 Designs for balloon/payload riggings with multiple tethers

We now propose a variety of rigging designs for tethered balloon/payload systems. As is customary in this application area, all strings will now be referred to as *tethers*. Also note that none of the designs proposed below are pretensionable (see §3.1.4), but most, with the notable exception of Design S1 in §4.2.1, are tensionable under load (see §3.1.5).

The main goal of the rigging design and tensioning system is to keep all tethers taut even as environmental disturbances act on the system, for three important reasons. First, a tensegrity structure with some tethers slack (thus, effectively absent as far as the forces within the structure are concerned) often exhibits additional soft modes, thus causing new infinitesimal mechanisms for substantial deflections of the structure in response to small disturbances in certain directions. Second, slack tethers are hazardous, as they can easily snag on various features on the payload or the ground. Finally, when slack tethers eventually become taut again, they often apply a sudden (possibly, damaging) "jerk" to the payload.

4.1 Initial 2D and 3D rigging designs

Before embarking, in §4.1.2, on a discussion/analysis of the initial 2D rigging concept proposed in Figure 2, we first note that it is straightforward to extend such 2D designs to 3D, using either threefold or fourfold symmetry, as illustrated in Figure 3 and discussed further in §4.1.1.

4.1.1 Threefold or fourfold symmetry of 3D balloon riggings

As noted above, it is straightforward to extend 2D rigging designs to 3D using either threefold symmetry, with 3 attachments nodes on both the balloon and payload, or fourfold symmetry, with 4 attachments modess on the balloon and payload. Further, note that some rigging designs we will consider, like those in Figures 2 and 3, isolate a superstructure (i.e., the balloon together with all tethers attached directly to it) from a substructure (i.e., the payload together with all tethers attached directly to it) via a convergence point (e.g., free node \mathbf{q}_5 in Figure 2). In the 3D versions of such designs, it is entirely possible to use threefold symmetry for the superstructure while using fourfold symmetry for the substructure, if the balloon used naturally has three attachment nodes but the payload used naturally has four attachment nodes, or vice versa. Note that, for rigging designs incorporating such a convergence point, we will also denote the balloon together with all tethers connecting it to the convergence point as the lower pyramid.

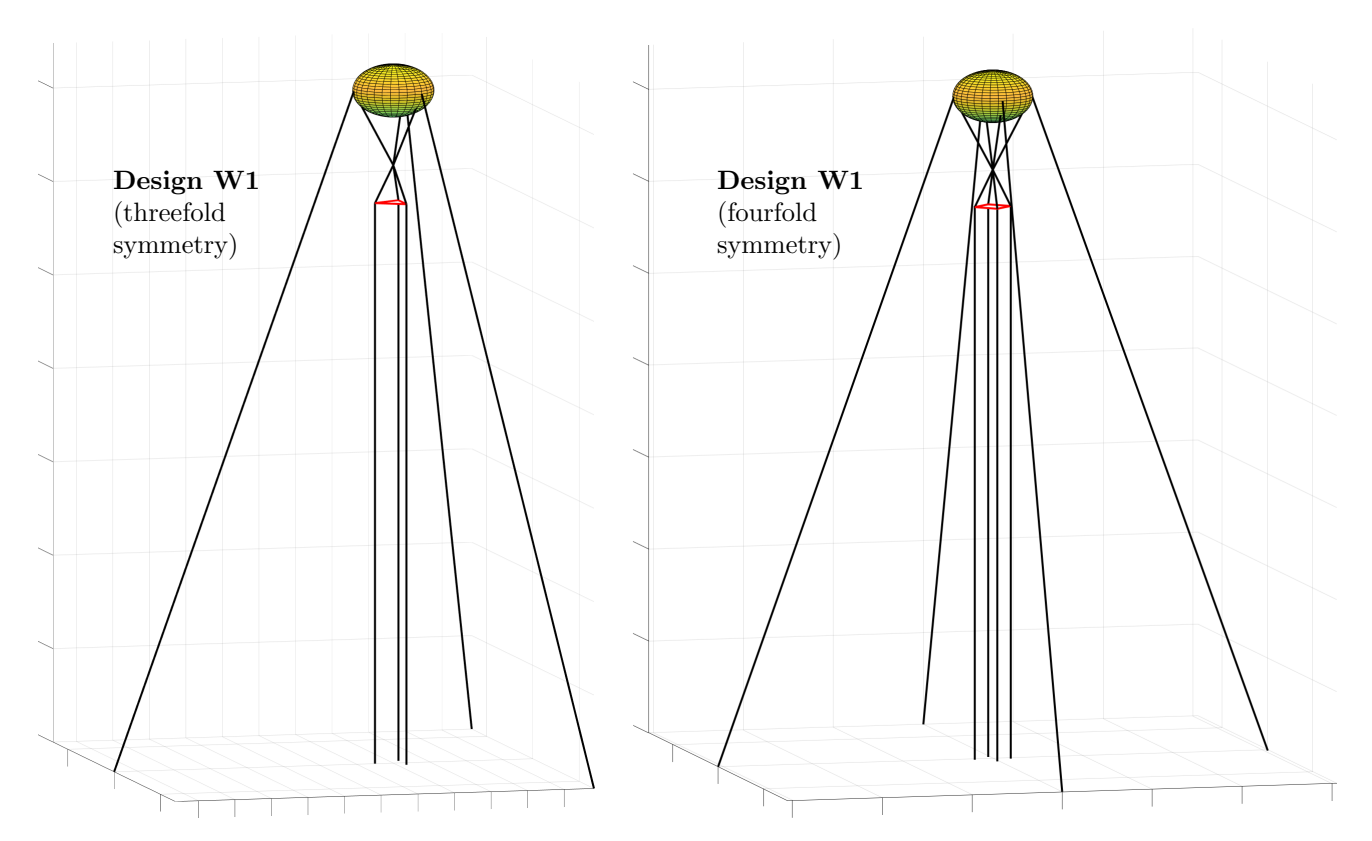


Figure 3: Two straightforward (albeit, still wobbly) extensions to 3D of the preliminary Design W1 of Figure 2 with (a) threefold symmetry, and (b) fourfold symmetry.

For simplicity, we will focus the bulk of the presentation below on 3D rigging configurations with threefold symmetry, noting that cases with fourfold symmetry represent straightforward extensions. Which symmetry is best to use in application is likely problem specific. Threefold symmetry uses fewer tethers, so it is less complicated and lighter. However, for a given payload height H and radius R of the ground attachment nodes, a square footprint on the ground subtends a substantially larger solid angle that an equilateral triangle footprint on the ground of the same radius. As discussed in the last paragraph of $\S 2$, the total load on the system (including disturbances) must generally remain within the solid angle formed by extending the lines formed by the ground tethers up above the balloon, in order to assure tensioning solutions exist that keep all ground tethers taut; designs with fourfold symmetry might therefore be more robust (and, thus, preferred) to those with threefold symmetry in applications for which the wind direction is variable.

4.1.2 Two useful features and one unfortunate liability of the initial 2D and 3D designs

The 2D and 3D versions of Design W1, as proposed in Figures 2 and 3, incorporate at least two distinctly useful features, both of which are incorporated into designs discussed later in §4, as well as one highly unfortunate liability (specifically, the presence of soft modes), which is eliminated in the major designs proposed in the subsections to follow. We now summarize both of these features, as well as this significant liability, in turn.

Feature 1: The use of a rigging design with a convergence point, with one or more pulleys incorporated, can effectively decouple the pitch (and, in 3D, the roll) of the balloon from the attitude of payload.

The use of a convergence point with a pulley system incorporated to isolate the attitude of the superstructure from that of the substructure is illustrated clearly/simply in 2D in Figure 2, and extends naturally to 3D (as depicted in Figure 3 and discussed in detail in §4.2.5). Given that, in reality, both the balloon and the tethers will all be somewhat elastic, and that, in most practical implementations, the balloon may be expected to undergo substantial environmental disturbances due to the wind, it might ultimately prove impossible to keep the balloon from deflecting somewhat in pitch, roll, and horizontal position, regardless of the rigging used (even when soft modes are eliminated, and feedback control is applied). The idea of using a convergence point to isolate these substantial balloon deflections from the attitude of the payload is thus, potentially, quite beneficial.

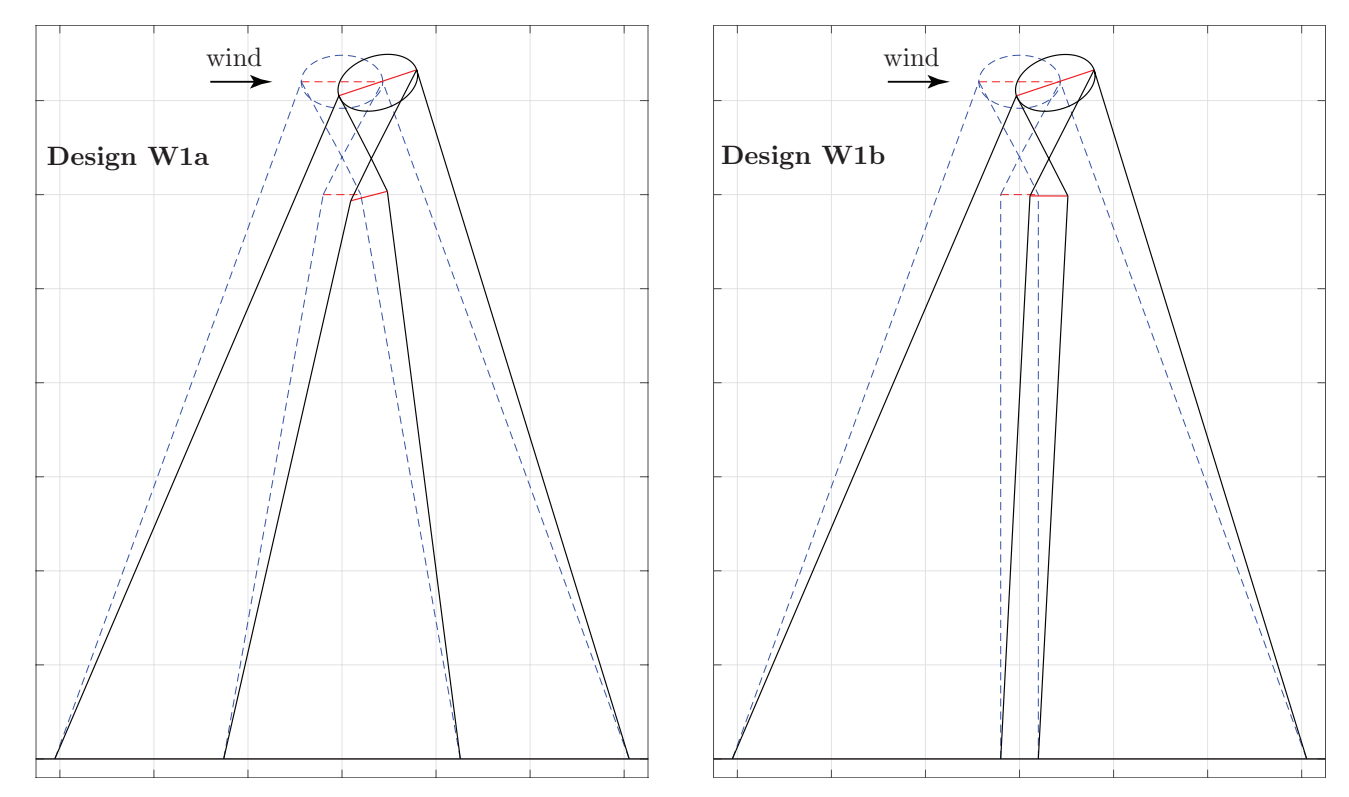


Figure 4: Substantial deflections of a balloon rigged with multiple ground tethers in the presence of wind, in the 2D setting of Figure 2, which is characterized by soft modes (see Liability in §4.1.2). (a) Design W1a, with tethers below payload angled to the ground, and (b) Design W1b, with tethers between the payload and ground taken as parallel. Unperturbed configuration is dashed, perturbed configuration (with wind from left) is solid. The pulley at the convergence point in both designs equalizes the tension of the left and right tethers in the upper pyramid, thereby isolating the pitching of the balloon from the attitude of the payload (see Feature 1 of §4.1.2). The 4-bar linkage between the payload and the ground in Design W1b forms a parallelogram which keeps the payload parallel to the ground, even as the convergence point shifts in horizontal position (see Feature 2 of §4.1.2).

Feature 2: The use of parallel tethers between the payload and the ground can assure geometrically (see, e.g., Figure 4) that, even if the convergence point (and, therefore, the payload) shifts a substantial amount horizontally (due to the various deflections of the balloon, which arise as a result of the wind disturbances acting upon the balloon), the pitch and roll of the payload will remain relatively undisturbed.

For the strategy described in Feature 2 to be effective, the following two conditions must be met:

- (i) the tethers between the payload and the ground must remain taut, and be of essentially equal length, and
- (ii) in the 3D case, the payload must not be substantially disturbed in yaw.

Applying the conditions of static equilibrium in (4b) of §3.1 to the 2D and 3D structures proposed in Figures 2, 3a, and 3b, it is found that all three of these structures are underdetermined. Though not pretensionable, all three of them turn out to be tensionable under load; that is, under nominal loading (applying the buoyancy of the balloon and the weight of the payload only), the tensions in the 2, 3, or 4 outer ground tethers can be adjusted (increased or decreased) with respect to the tensions in the 2, 3, or 4 inner ground tethers, thus providing one degree of freedom that may be leveraged to attempt to assure that condition (i) is satisfied. Note that, in order to maintain the (parallel) inner tethers at nearly equal length, any tether tensioners (i.e., winches used to adjust the tensions in the system) to be implemented should be applied to the outer tethers.

Unfortunately, the conditions of static equilibrium in (4b) are also *potentially inconsistent*, revealing the following: **Liability**: The 2D and 3D structures proposed in Figures 2 and 3 contain soft modes involving deflections of the attitude and horizontal position of the balloon in response to disturbances. Additionally, the 3D structures proposed in Figure 3 contain soft modes involving deflections in the yaw of the payload.

Such soft modes imply that these structures will suffer substantial deflections in response to small disturbances in certain directions. This liability removes these three wobbly structures from further serious consideration. Better rigging designs that eliminate such soft modes are available, as proposed next.

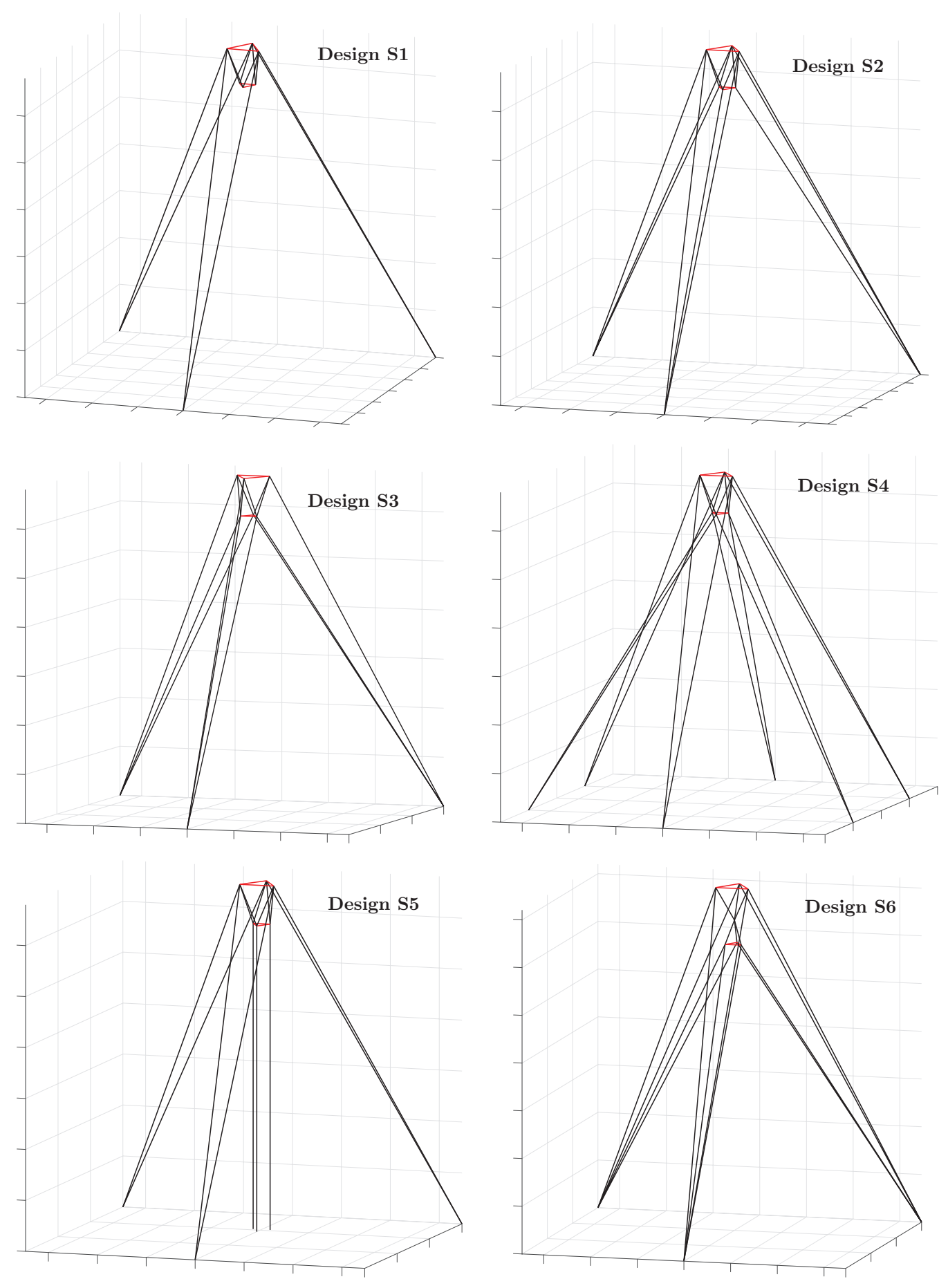


Figure 5: The six stable 3D rigging designs considered in $\S 4$ using 3-fold symmetry (designs with 4-fold symmetry are similar); none have soft modes. For clarity, the balloon is depicted as a triangle of bars in these sketches.

4.2 Stable 3D rigging designs for practical use

Note, as mentioned previously, that we will focus the presentation below on 3D rigging configurations with threefold symmetry, noting that cases with fourfold symmetry represent straightforward variations (and which, indeed, are in some cases preferred).

4.2.1 Design S1: eliminating soft modes

Design S1 in Figure 5, with six ground tethers and only three (fixed) ground nodes, has no soft modes. By using six ground tethers rather than three (i.e., by using two ground tethers from each balloon attachment node rather than one, with these two tethers forming as wide a footprint on the ground as possible without crossing the other tethers, thus meeting at just three ground nodes), Design S1 can withstand small disturbances on all nodes from all directions without deflection, assuming non-stretchable tethers. This design is statically determinant, i.e.:

- the six DOF of the balloon are held in place by the six tethers from the balloon to the ground, and
- the six DOF of the payload are held in place by the six tethers from the payload to the balloon.

Design S1 has no additional degrees of freedom; in static equilibrium, the tensions in the tethers are determined entirely by the (nominal and disturbance) loads. Though simplifying the analysis and implementation, this feature also eliminates the flexibility that one achieves with an underdetermined (tensionable) static equilibrium. This tradeoff is analyzed further in §4.5.

Note that the tethers between the (idealized) bars representing the balloon and the payload form a triangular antiprism (a.k.a. an octahedron¹⁴). With a triangle on every face, such an polyhedron is easily recognized as a strong structural element, especially if the member lengths are such that this polyhedron is nearly regular.

To summarize, Design S1 in Figure 5, with six ground tethers to just three fixed nodes on the ground, is the simplest practical starting point for rigging a balloon/payload system with no soft modes. A straightforward variant of Design S1 attaches the payload to the ground (again, with six tethers) instead of attaching the balloon to the ground; a possible rationale for such a variant is discussed in the second paragraph of §4.2.2.

4.2.2 Designs S2, S3, S4: adding tethers for additional flexibility in tensioning

Starting from the (statically-determinant) Design S1, we now pursue the idea of adding additional tethers, thus giving additional flexibility in the tensioning of the structure once the nominal loads are applied. If we consider using three ground nodes and three tethers per ground node, there are two natural options. The first option (Design S2 in Figure 5) is simply to add three ground tethers to Design S1, one from each payload attachment node to the nearest ground node. The second option (Design S3 in Figure 5), is essentially the inverse: to use two ground tethers from each attachment node on the payload, and one ground tether from each attachment node on the balloon. Both designs have $\overline{n} = 3$ extra degrees of freedom in their static equilibrium (i.e., the corresponding \overline{V} in §3.1.4 has three columns); thus, once loaded, substantial flexibility in the tension distribution is possible with these designs, and three independent tether tensioners may be implemented while not disrupting the static equilibrium.

Since the balloon (with its large exposed surface area) undergoes the largest disturbances from the wind and is likely somewhat soft, and the priority is to stabilize the payload, Design S3, with the six DOF of the payload directly stabilized by six ground tethers, is anticipated to be somewhat better than Design S2 in practice. Note that the wider the radius of the payload (a triangle in these designs), the greater the available moment arm for generating correction torques by the tethers, and the better the stability in attitude of the payload.

Taking the idea of additional tethers one step further, Design S4 in Figure 5 uses two ground tethers per balloon attachment point, and two ground tethers per payload attachment point, thereby introducing $\overline{n}=6$ extra degrees of freedom in the static equilibrium. Forming as wide a footprint on the ground as possible in this configuration without crossing tethers leads, as shown, to six ground nodes rather than three, which presents somewhat of a complication in the implementation. This design also, however, substantially increases the solid angle subtended by the ground tethers from the balloon/payload system (see the last paragraphs of §2 and §4.1.1), thereby potentially increasing the robustness of this design as compared with Designs S2 and S3.

4.2.3 Design S5: reintroducing parallel ground tethers from the payload

Design S5 in Figure 5 modifies Design S2 by making the three ground tethers from the payload parallel, thereby reintroducing Feature 2 of §4.1.2, geometrically assuring stiffness of the payload to pitch, roll, and vertical translations.

 $^{^{14}}$ In the case of fourfold symmetry, the tethers between the (idealized) bars representing the balloon and the payload form a square antiprism.

This design has $\overline{n} = 3$ extra degrees of freedom (again, best adjusted on the outer ground tethers, in order to keep the inner ground tethers of essentially equal length). This design also has six ground nodes, though the three inner ground nodes would likely all be attached to a single structure, or vehicle, of the same radius as the payload.

4.2.4 Design S6: reintroducing the convergence point using a 3D pulley system

Design S6 in Figure 5 reintroduces the use of a convergence point to isolate the possible pitching and rolling of the balloon (which is expected to undergo significant deflections, due to its large exposed surface area and its compliance, as well as the elasticity of real tethers, even in rigging designs with no soft modes) from the attitude of the payload. As in Design W1, to facilitate this isolation, a pulley system should be incorporated into the three tethers connecting the balloon to the convergence point (i.e., in the upper pyramid), thereby equalizing their tensions. The interesting problem of how best to configure these pulleys in this case is discussed in detail in §4.2.5 below.

Note that, with this pulley system installed, there is one remaining tension DOF in Design S6, implying that one tether tensioner can be used. Note also that, with the payload rotated by 60° as compared with Designs S2-S5, Design S6 again uses only 3 ground attachment nodes.

4.2.5 The upper pyramid

In the case of fourfold symmetry of the superstructure (e.g., in Design W3 of Figure 3), the problem of equalizing the tension of the four tethers of the upper pyramid is trivial: at the convergence point, simply implement a single (lightweight) piece of hardware, easily fabricated within a small piece of aluminum square tube (see Figure 6e), with:

- one small pulley (a.k.a. U-groove bearing) in the x-z plane, to equalize the tensions of the left/right tethers of the upper pyramid),
- \bullet one small pulley in the y-z plane, mounted immediately above the other pulley, to equalize the tensions of the front/back tethers of the upper pyramid, and
- a suitable set of tie-down points immediately below the pulleys to attach the (3 or 4) tethers supporting the payload in the lower pyramid.

However, in the case of threefold symmetry of the superstructure (e.g., in Design W2 of Figure 3, and Design S6 of Figure 5), the problem of equalizing the tension of the three tethers in the upper pyramid is substantially more delicate. In this case, if arranged symmetrically (generally the goal, for both balancing the forces applied to the balloon, and for simplicity of construction), the three tethers extending down from the balloon to the convergence point in fact form a regular triangular pyramid. Such a pyramid has a base (actually, a top) which may be visualized as an equilateral triangle, and the three tethers leading down from the balloon form the remaining edges of three congruent isosceles triangles as lateral faces. Denote the height of this pyramid as h, the radius (around the vertical axis) of the 3 attachment points of the tethers to the balloon as r, the convergence point as B, and the tensions in the three tethers as τ_1 , τ_2 , and τ_3 . It follows from simple geometry (see Figure 6a) that:

- (a) the three edges of the base (modelled as bars) each have length $a = r\sqrt{3}$,
- (b) the three tethers (strings) are each of length $b = \sqrt{h^2 + r^2}$,
- (c) the angle at B between the vertical axis and any of the tethers is $\alpha = \tan^{-1}[r/h]$,
- (d) the angle at B between the vertical axis and the plane containing any 2 of the tethers is $\beta = \tan^{-1}[r/(2h)]$,
- (e) the angle at B between any 2 of the tethers is $\gamma = 2 \sin^{-1}[a/(2b)]$, and
- (f) the total lift force provided to the load is $L = (\tau_1 + \tau_2 + \tau_3) \cos \alpha$.

We now describe three small pieces of hardware (again, all easily fabricated using small pulleys and small pieces of aluminum plate), to be implemented at positions T1, T2, and B (see Figure 6), to approximately equalize the tensions in the three tethers coming down from the balloon. We start by equalizing τ_1 and τ_3 via a simple pulley at T1; it is said that such a configuration is MA1 (Mechanical Advantage 1), so that the tensions τ_1 and τ_3 in the tethers on either side of T1 equalize. We then aspire to somehow attach tether 2 to both B (that is, the convergence point), which supports the load, and T1, which connects to tethers 1 and 3, in such a manner that $\tau_2 \approx \tau_1 = \tau_3$, and thus the upper pyramid remains nearly regular.

If $h \ll r$, we can follow the simplest (MA1) approach again, just routing tether 2 through a simple pulley at B and tying it off at T1 (see Figure 6b). In this MA1 configuration between τ_2 and T1, if $h \ll r$ and thus $\gamma \approx 120^\circ$, we obtain $\tau_2 \approx \tau_1 = \tau_3$. Unfortunately, taking $h/r \to 0$ also makes $\alpha \to 90^\circ$ and thus, by point (f) above for fixed L, $\tau_i \to \infty$; this is thus, clearly, not a viable approach. For larger h in this MA1 configuration, τ_2/τ_1 increases (approaching $\tau_2/\tau_1 \approx 2$ for $h \gg r$), and thus the forces in the upper pyramid are out of balance until a new equilibrium is reached, with angles at the convergence point that are significantly different from those of the (desired) regular triangular pyramid, as summarized above.

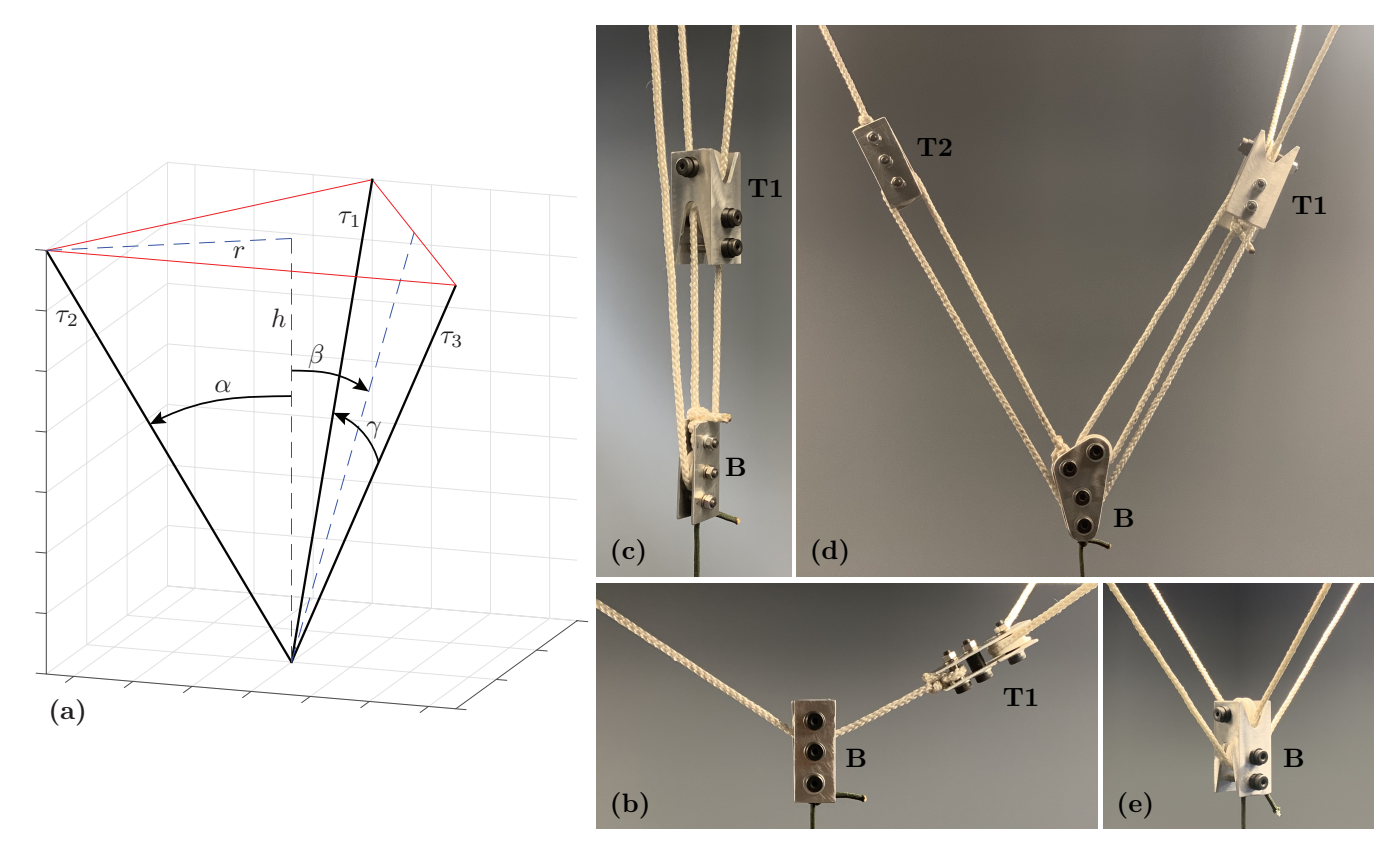


Figure 6: Geometry and representative hardware (B, T1, T2) of the pulley system near the convergence point of the upper pyramid of Designs C and D in Figure 5, designed to isolate the pitching/rolling of the balloon from that of the payload while equalizing the tensions $\{\tau_1, \tau_2, \tau_3\}$, in the case of threefold symmetry: (a) notation used, (b) MA1 between τ_2 and T1 (suitable for $h \ll R$), (c) MA2 between τ_2 and T1 (suitable for $h \gg R$), (d) MA1.5 between T2 and T1 (best suited for $h/r \approx 0.845$). Also shown, in (e), is the single piece of hardware sufficient to stabilize left/right tensions and fore/aft tensions in the (simpler) case of fourfold symmetry.

If $h \gg r$, on the other hand, we can instead route tether 2 through a pulley at B and a second pulley at T1, and then tie this tether off at back at B (see Figure 6c). In this MA2 configuration between τ_2 and T1, if $h \gg r$, we again obtain $\tau_2 \approx \tau_1 = \tau_3$. Unfortunately, taking $h/r \to \infty$ diminishes the lateral stability of the convergence point (and, thus, the payload) in the presence of horizontal disturbances acting on the payload. For smaller h in this MA2 configuration, τ_2/τ_1 decreases (approaching $\tau_2/\tau_1 \approx 1/2$ for $h \ll r$), and thus, again, the forces in the upper pyramid are out of balance until a new equilibrium is reached with angles at the convergence point that are significantly different from those of a regular triangular pyramid.

A single block-and-tackle arrangement, like the proposed connections between the top block T1 and the bottom block B as discussed above, can only achieve an integer MA. We saw that an MA1 arrangement was suitable for $h \ll r$, and that an MA2 arrangement was suitable for $h \gg r$. For intermediate values of h/r, both arrangements lead to forces that are significantly out of balance at the convergence point until a new equilibrium is reached, with angles that are significantly different from those of the desired regular triangular pyramid centered below the balloon.

What we seek is a mechanical advantage between the tension τ_2 and the force on the hardware at point T1 in the direction of B that is somewhere between MA1 and MA2. To achieve this, consider inserting a second top block, T2, somewhere along tether 2 between point B and the balloon, as shown in Figure 6d. By implementing an MA3 pulley configuration from T1 to B, and an MA2 pulley configuration from B to T2, a total mechanical advantage of 3/2=1.5 is achieved¹⁵. If $\gamma = 2\cos^{-1}(3/4) \approx 82.82^{\circ}$ and thus $a/b = 2\sin(\gamma/2) \approx 1.323$ and $b/r = \sqrt{3/(a/b)^2 - 1} \approx 0.845$,

 $^{^{15}}$ Implementing different integer coprime mechanical advantages, MAm and MAn, in the two attached block and tackle systems (from T1 to B, and from B to T2, in Figure 6d), by incorporating more pulleys, leads directly to the possibility of achieving different fractional mechanical advantages, MA(m/n), though doing such appears to be unnecessary in the present application. The use of (usually) equal-diameter pulleys in a block and tackle arrangement to achieve integer MA is well known, as is the use of different-diameter pulleys in a wheel and axle arrangement to achieve non-integer MA; documented discussion of both dates back at least to Hero of Alexandria in the first century AD. As far as we can tell, however, Figure 6d and its generalization discussed here apparently documents the first use of two interconnected block and tackle systems to achieve fractional MA (between T1 and T2) using equal-diameter pulleys.

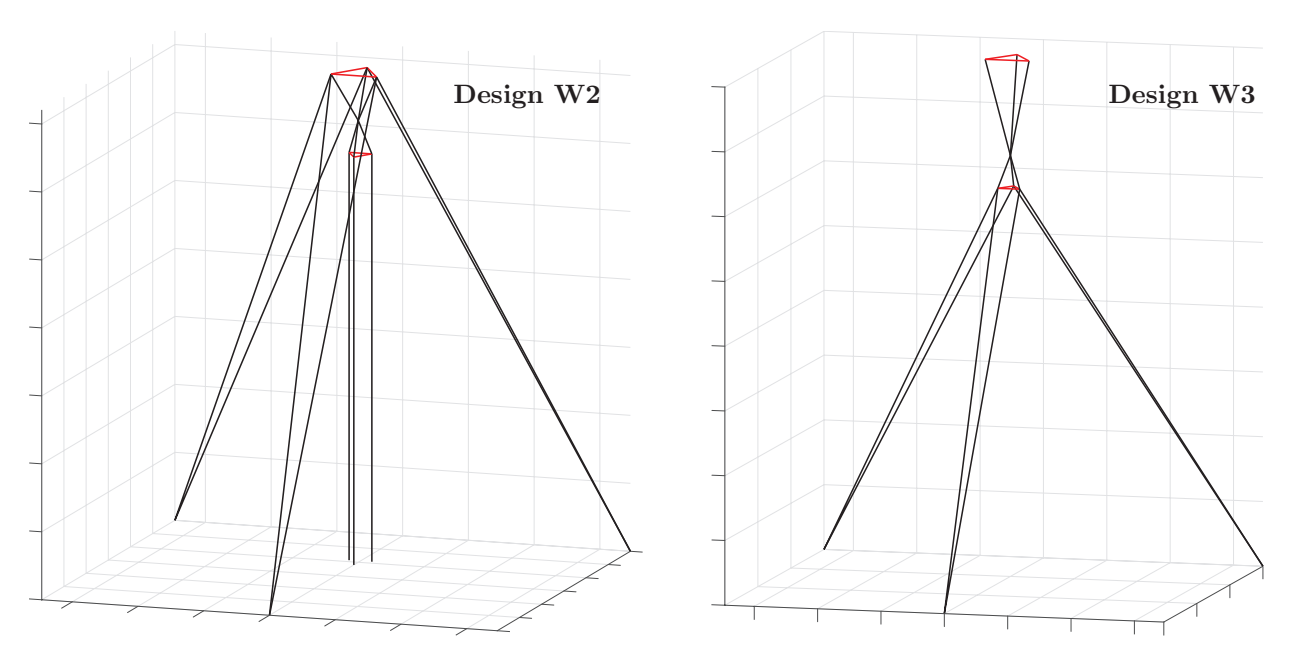


Figure 7: Two rigging designs that are *not* recommended: (left) combining the ideas of using a convergence point and using parallel tethers from the payload to the ground, and (right) giving up completely on stabilizing the balloon position/orientation. Both designs have soft modes.

which is reasonable ¹⁶, this MA1.5 configuration obtains the desired balance, with $\tau_1 = \tau_2 = \tau_3 \approx 0.516 L$.

To summarize, for the threefold case, we recommend an MA1.5 pulley configuration, as shown in Figure 6d and introduced above, together with an aspect ratio for the (regular triangular) upper pyramid of about $h/r \approx 0.845$.

4.2.6 The lower pyramid

If one can guarantee that all of the tethers between the payload and the ground will always stay taut in Designs W1, W2, W3, or S6, the idea of using pulleys to equalize the tension in the tethers in the upper pyramid, as discussed in §4.2.5, might also be considered for the lower pyramid. However, in operation, we can usually not make such an absolute guarantee, as large wind gusts might occasionally, unfortunately, make one or more of these ground tethers go slack. If/when this happens, even for a short period of time, the orientation of the payload will go unstable if pulleys are incorporated in the lower payload, and the subsequent sudden jerk of the payload after it falls over to one side might likely cause significant damage.

Thus, it is *not* recommended to use a pulley system in the lower pyramid; instead, the convergence point should just be connected directly to the (2, 3, or 4) corners of the payload with individual tethers. An equilateral triangle (in 2D), equilateral triangular pyramid (a.k.a. a regular tetrahedron), or equilateral square pyramid would be typical reasonable choices.

4.3 Other wobbly rigging designs (not recommended)

Many other "wobbly" rigging designs, with infinitesimal modes leading to substantial structural deflections in response to small wind disturbances, are possible; for completeness, two additional wobbly designs are discussed briefly here. Our general advice is to avoid all such soft designs in favor of stable rigging configurations, like Designs S1-S6 in Figure 5, and variants of these designs with fourfold symmetry.

4.3.1 Design W2: implementing a convergence point and parallel tethers from payload to ground

Design W2 in Figure 7 combines the ideas of using a convergence point, as in Design S6, and using parallel tethers from the payload to the ground, as in Design S5. Unfortunately, such a design is soft to disturbance forces in yaw applied to the payload itself (though the rigging of the balloon itself is not soft). To counter this fact, one might propose adding a reaction-wheel stabilization system (the design and implementation of which is well understood, and need not be expensive or complicated) in order to recover payload stability in yaw. Such reaction wheel stabilization

¹⁶That is, this is reasonable in terms of both the magnitude of τ (cf. the MA1, $h \ll R$ case) and the lateral stability of the convergence point in the presence of disturbances on the payload (cf. the MA2, $h \gg R$ case).

systems provide reaction torque, on demand, to the body to which they are mounted simply by using motor(s) to apply torque to wheel(s) with significant rotational inertia.

Unfortunately, to realize the required rotational inertia, reaction wheels generally have a significant amount of dead weight associated with them; this added weight on a payload reduces the excess lift E that is critical to the stability of the balloon/payload system in light of external wind forces, as described in §2. In contrast, tensioners on the ground tethers in Designs S1-S6 can be placed on the ground, and thus static tensioning and/or active control using such tensioners doesn't impact the excess lift calculation at all. Even tensioners on the tethers between the payload and the balloon in these designs are, likely, better overall than implementing reaction wheel systems, as they do not have the dead weight associated with reaction wheels.

4.3.2 Design W3: abandoning balloon stabilization altogether

Another alternative strategy, illustrated by Design W3 in Figure 7, gives up on stabilizing the position and orientation of the balloon altogether, instead focusing solely on stabilizing the payload, while allowing the balloon to move to and fro as it may (through a convergence point isolating the balloon orientation from the payload orientation, as discussed previously). This approach is perhaps reasonable if the disturbances from the wind are relatively steady. One of the chief concerns in the present effort, however, is the possibility of sympathetic forcing of the balloon via alternate vortex shedding due to the wind past the balloon [1], possibly leading to very large oscillations of the balloon position even in relatively light winds (for an example of this phenomenon, see [22]). For this reason, we are not optimistic about this design approach. If it is attempted, subduing these oscillations by periodically varying the effective length of the (inverted) pendulum leading up to the balloon, via synchronized adjustment of the lengths of all three tethers in the upper pyramid using the strategy proposed in [1], might well be beneficial.

4.4 Modified designs for cliff exploration

Figure 8 indicates three representative riggings (Designs C1, C2, and C3) for cliff exploration, as proposed in §1.1. All three are natural generalizations of Design S2 introduced in §4; a host of related variants are also possible. All three variants shown include:

- two tethers to the balloon from each of three or four fixed or mobile ground points above and below the cliff, thereby securing all six DOF of the balloon with no soft modes,
- a (triangular or square) right antiprism suspending the payload from the balloon, together with
- one extra tether to the closest corner of the payload from each of the ground points below the cliff.

Note that tethers to the payload from the ground points above the cliff are omitted in these designs, to avoid such tethers from getting snagged on ground features. Note also that the use of more than three ground points in such applications is potentially beneficial, as it increases the area over which the balloon and payload can stably explore before having to move the ground points.

4.5 Future work

A Github repository with a new Matlab codebase fully implementing the dynamic equations of §3.1 and 3.2, allowing (apparently, for the first time) the general embedding of solid bodies with specified mass distributions and specified nodal attachment points into class 1 tensegrity systems, is available at:

https://github.com/tbewley/TenSim

Included in this repository are all of the new balloon + payload rigging designs proposed in the present paper as examples, where both the balloon and the payload are modelled as solid bodies. For space considerations, numerical simulations of the dynamics these new balloon + payload rigging designs, as well as various other related systems that embed solid bodies into tensegrity structures, leveraging this new formulation and codebase, will be characterized extensively in a follow-up paper, comparing numerical simulations with corresponding experimental results.

Acknowledgements

The author gratefully acknowledges the financial support of JPL, Caltech, under a contract with NASA in support of this work, and would like to personally thank Fred Hadaegh, David Hanks, Adrian Stoica, S. Ryan Alimo, and Mike Pauken at JPL for their support of this effort. The author also gratefully acknowledges Mauricio de Oliveira for helpful advice related to the dynamics of tensegrity structures, Paolo Luchini for helpful discussions regarding the balloon Froude number, Kurt Talke and Eric Sihite for machining the hardware used in Figure 6, and collaboration

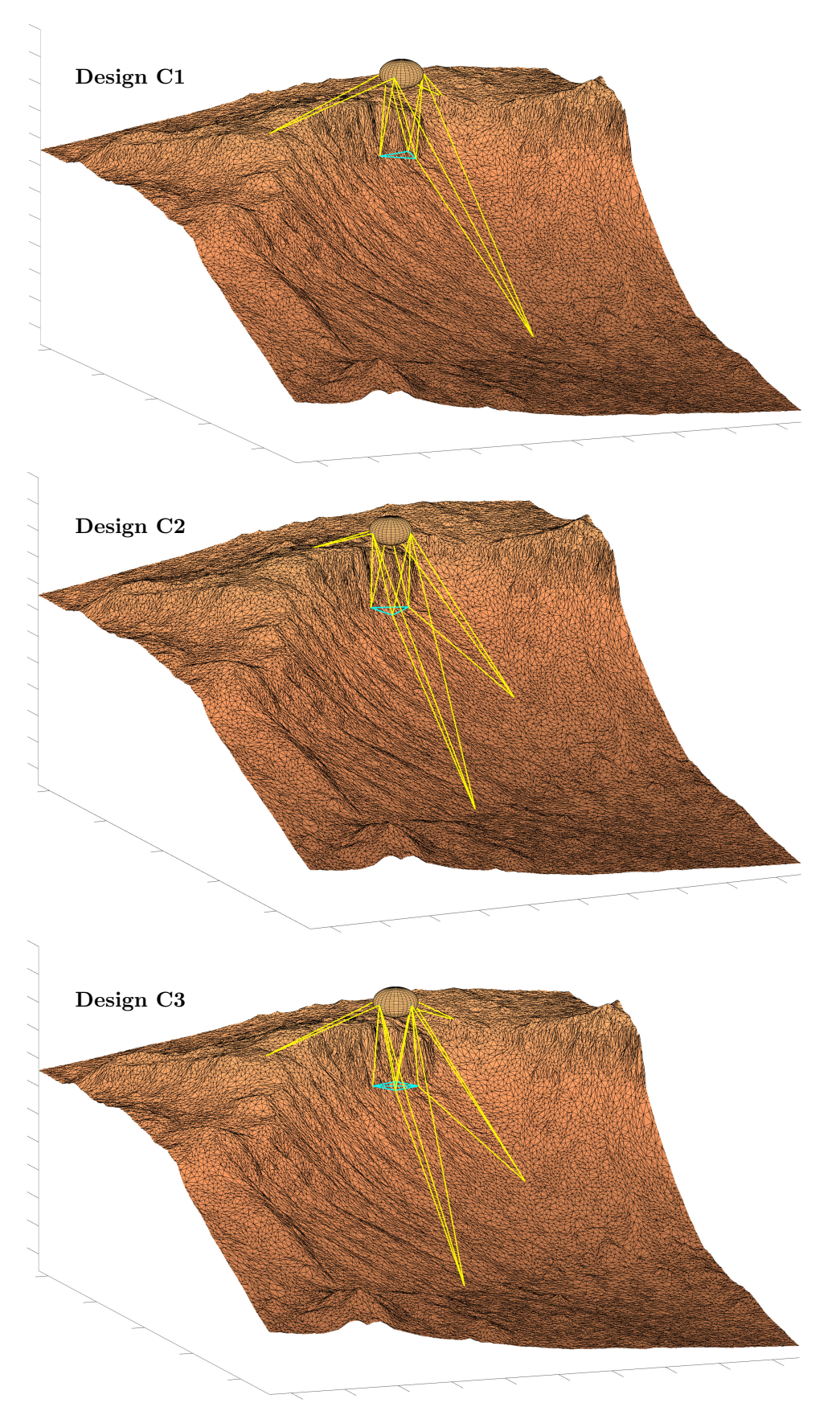


Figure 8: Three potential deployment scenarios for a remote observation platform suspended over a cliff from a balloon tethered to fixed or mobile ground attachment points. Topographic model of the western region of Hale Crater from the High Resolution Imaging Science Experiment (HiRISE) on the Mars Reconnaissance Orbiter, available at [21].

with Adrian Stoica, S. Ryan Alimo, Chrishma Derewa, Hunter Hall, Mike Lally, Christine Yuan, Luan Nguyen, and Kyle Weng on the balloon-based science experiment illustrated in Figure 1a.

References

- [1] Bewley, T (2020) Stabilization of low-altitude balloon systems, Part 1: rigging with a single taut ground tether, analyzed as a variable-length pendulum. Submitted.
- [2] Bretl, T., Rock, S., Latombe, J.-C., Kennedy, B, & Aghazarian H. (2006) Free-Climbing with a Multi-Use Robot, Experimental Robotics IX, 449-458.
- [3] Cavaglieri, D., & Bewley, T.R. (2015) Low-storage implicit/explicit Runge-Kutta schemes for the simulation of stiff high-dimensional ODE systems, *Journal of Computational Physics* **286**, 172-193.
- [4] Dasaradhan, B., Das, B.R., Sinha, M.K., Kumar, K, Kishore, B, & Prasad, N.E. (2018) A Brief Review of Technology and Materials for Aerostat Application. *Asian Journal of Textile* 8, 1-12.
- [5] de Jong, M (2015) Venus altitude cycling balloon. Proceedings of the Venus Science Priorities for Laboratory Measurements and Instrument Definition Workshop, (April 7-8, Hampton, Virginia), p. 4030.
- [6] de Oliveira, M., Vera, C., Valdez, P., Sharma, Y., Skelton, R.E., & Sung, L.A. (2009) Nanomechanics of Multiple Units in the Erythrocyte Membrane Skeletal Network, *Annals of Biomedical Engineering* **38** (9), 2956-2967.
- [7] Garcia, M.B., Espadaler, X, & Olesen, J.M. (2012) Extreme Reproduction and Survival of a True Cliffhanger: The Endangered Plant Borderea chouardii (Dioscoreaceae). *PLoS ONE* **7** (9): e44657.
- [8] Hall, J.L., Cameron, J.M., Pauken, M.T., Izraelevitz, J.S., Dominguez, M.W., Wehage, K.T. (2019) Altitude-Controlled Light Gas Balloons for Venus and Titan Exploration AIAA AVIATION Forum, 17-21 June, Dallas.
- [9] Kolb, K.J., Pelletier, J.D., McEwan, A.S. (2010) Modeling the formation of bright slope deposits associated with gullies in Hale Crater, Mars: Implications for recent liquid water. Icaras **205** (1), 113-137.
- [10] de Oliveira, M. (2006) Dynamics of Systems with Rods IEEE Conference on Decision & Control, 2326-2331.
- [11] Masic, M., Skelton, R.E., & Gill, P.E. (2006) Optimization of tensegrity structures. *International Journal of Solids and Structures* **43** (16), 4687-4703.
- [12] Meirovitch, L. (1970) Methods of Analytic Dynamics. McGraw-Hill.
- [13] Meneghello, G., Bewley, T.R., de Jong, M., & Briggs, C. (2017) A coordinated balloon observation system for sustained in-situ measurements of hurricanes. IEEE Aerospace Conference, Big Sky.
- [14] Nesnas, I.A.D., Matthews, J.B., Abad-Manterola, P., Burdick, J.W., Edlund, J.A., Morrison, J.C., Peters, R.D., Tanner, M.M., Miyake, R.N., Solish, B.S., & Anderson, R.C. (2012) Axel and DuAxel rovers for the sustainable exploration of extreme terrains *Journal of Field Robotics* 29 (4) 663-685.
- [15] Shabana, A.A. (2003) Dynamics of Multibody Systems. Cambridge University Press, 2nd ed..
- [16] Skelton, R.E., & de Oliveira, M.C. (2009) Tensegrity Systems. Springer.
- [17] Stoica, A, et al. (2016) WindBots NIAC Phase I Final Report. Available at: https://www.nasa.gov/sites/default/files/atoms/files/niac_2015_phasei_stoica_windbots_tagged.pdf
- [18] Talke, K.A., de Oliveira, M., & Bewley, T. (2018) Catenary Tether Shape Analysis for a UAV USV Team IROS, 7803-7809.
- [19] Townsend, I., Muscatello, A.C., Dickson, D., Sibille, L., Nick, A., Leucht, K., & Tamasy, G. (2017) Mars ISRU Pathfinder Regolith Autonomous Operations Modeling and Systems Integration *Proceedings, AIAA SPACE and Astronautics Forum and Exposition*, 12-14 Sep. Orlando.
- [20] Voss, P.B., Riddle, E.E., & Smith, M.S. (2005) Altitude control of long-duration balloons, AIAA Journal of Aircraft 42 (2), 478-482.
- [21] Bright Gully Deposits in Western Hale Crater. Available at: https://hirise.lpl.arizona.edu/ESP_013019_1450

[22] Fox5 News, Feb 19, 2019, San Diego, Riders survive terrifying wind-whipped balloon ride at Safari Park. Available at: https://fox5sandiego.com/2019/02/19/women-kids-survive-terrifying-balloon-ride-at-safari-park/